# Flexible Intelligent Metasurfaces for Downlink Multiuser MISO Communications

Jiancheng An, *Member, IEEE*, Chau Yuen, *Fellow, IEEE*, Marco Di Renzo, *Fellow, IEEE*, Mérouane Debbah, *Fellow, IEEE*, H. Vincent Poor, *Life Fellow, IEEE*, and Lajos Hanzo, *Life Fellow, IEEE*

***Abstract*—Flexible intelligent metasurface (FIM) technology shows promise in terms of enhancing both the spectral and energy efficiency of wireless networks. An FIM is composed of an array of low-cost radiating elements, each of which can independently radiate electromagnetic signals, while flexibly adjusting its position along the direction perpendicular to the surface by a process termed as "morphing". This is of particular interest for wireless communication systems operating at Terahertz frequencies, where deep fading generally occurs within a few millimeters. Hence, in contrast to conventional rigid 2D antenna arrays, the FIM surface shape may be reconfigured to improve the channel quality by beneficial 3D morphing. In this paper, we investigate the multiuser downlink, where an FIM deployed at a base station (BS) communicates with multiple single-antenna users. We formulate an optimization problem for minimizing the total downlink transmit power at the BS, by jointly optimizing the transmit beamforming and FIM surface shape, subject to an individual signal-to-interference-plus-noise ratio (SINR) constraint of each user as well as a constraint on the maximum FIM morphing range. To solve this problem, we first consider a simple single-user scenario and show that the optimal 3D surface shape is achieved by independently adjusting each FIM element to the position having the strongest channel gain. However, in realistic multiuser scenarios, FIM surface-shape morphing involves complex tradeoffs. To address this issue, an efficient alternating optimization method is proposed to iteratively update the FIM surface shape and the transmit beamformer to gradually reduce the transmit power. Additionally, we analyze the performance gain of the FIM, showcasing a logarithmic received power scaling law versus its maximum morphing range. Finally, simulation results show that the FIM reduces the transmit power by about 3 dB compared to conventional rigid 2D arrays at a given data rate[1].**

***Index Terms*—Flexible intelligent metasurface (FIM), transmit beamforming, surface-shape morphing, MIMO, intelligent surfaces.**

This research is supported by the Ministry of Education, Singapore, under its MOE Tier 2 (Award number MOE-T2EP50220-0019), National Research Foundation, Singapore, and Infocomm Media Development Authority under its Future Communications Research & Development Programme FCP-NTU-RG-2024-025. The work of M. Di Renzo is supported in part by the European Commission through the Horizon Europe project COVER under grant agreement number 101086228, the Horizon Europe project UNITE under grant agreement number 101129618, and the Horizon Europe project INSTINCT under grant agreement number 101139161, as well as by the Agence Nationale de la Recherche (ANR) through the France 2030 project ANR-PEPR Networks of the Future under grant agreement NF-YACARI 22-PEFT-0005, and by the CHIST-ERA project PASSIONATE under grant agreements CHIST-ERA-22-WAI-04 and ANR-23-CHR4-0003-01. H. V. Poor would like to acknowledge the U.S National Science Foundation under Grant ECCS-2335876. L. Hanzo would like to acknowledge the financial support of the Engineering and Physical Sciences Research Council (EPSRC) projects under grant EP/Y037243/1, EP/W016605/1, EP/X01228X/1, EP/Y026721/1, EP/W032635/1, EP/Y037243/1 and EP/X04047X/1 as well as of the European Research Council's Advanced Fellow Grant QuantCom (Grant No. 789028). *(Corresponding author: Chau Yuen)*

J. An and C. Yuen are with the School of Electrical and Electronics Engineering, Nanyang Technological University, Singapore 639798 (e-mail: jiancheng.an@ntu.edu.sg, chau.yuen@ntu.edu.sg). M. Di Renzo is with Université Paris-Saclay, CNRS, CentraleSupélec, Laboratoire des Signaux et Systèmes, 3 Rue Joliot-Curie, 91192 Gif-sur-Yvette, France (e-mail: marco.direnzo@universite-paris-saclay.fr). M. Debbah is with Khalifa University of Science and Technology, P O Box 127788, Abu Dhabi, UAE (e-mail: merouane.debbah@ku.ac.ae). H. V. Poor is with the Department of Electrical and Computer Engineering, Princeton University, Princeton, NJ 08544, USA (e-mail: poor@princeton.edu). L. Hanzo is with the School of Electronics and Computer Science, University of Southampton, Southampton SO17 1BJ, U.K. (e-mail: lh@ecs.soton.ac.uk).

## I. Introduction

NEXT-GENERATION wireless networks aim for supporting many innovative applications, such as brain-computer interfaces, high-fidelity holograms, connected robotics, and autonomous vehicles [1]. However, these applications entail very stringent quality-of-service (QoS) demands, including extremely high data rates, ubiquitous and ultra-reliable connectivity, as well as ultra-low latency [2], which cannot be readily achieved by the current network infrastructure. While deploying large numbers of antennas and base stations operating at higher frequencies having ample bandwidth could meet these goals, both the energy consumption and hardware costs of such solutions would be excessive. To balance these challenging QoS requirements against energy efficiency, researchers have developed sophisticated wireless technologies over the past decade. Among them, the emerging metasurface technology is regarded as one of the most promising solutions [3]–[6].

Generally speaking, a metasurface is an artificially engineered planar surface constructed of an array of tiny meta-atoms [3]. Each meta-atom is capable of independently radiating or scattering wireless signals by beneficially modifying the properties of electromagnetic (EM) waves, such as their amplitudes, phases, and polarizations [5]. In recent years, deploying near-passive reconfigurable intelligent surfaces (RISs) in wireless networks has shown significant potential for shaping wireless propagation environments [7]. For example, in indoor scenarios, installing RISs on walls or ceilings can circumvent the blockage of the line-of-sight (LoS) propagation link between a WiFi access point and a mobile device [8], hence significantly increasing the received signal strength. Since RISs interact with incoming signals without requiring power amplifiers and complex signal processing, they avoid the costly radio frequency (RF) hardware of conventional active transceivers [4].

[1]The code for this paper is available at https://github.com/JianchengAn.

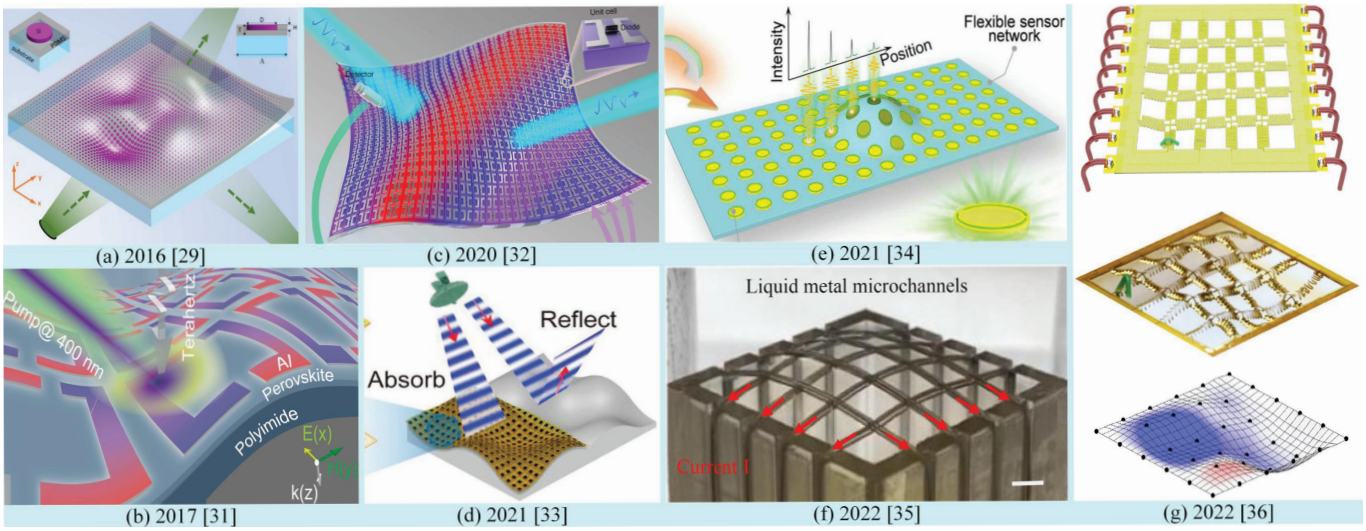


Fig. 1. Illustration of some existing FIMs.

While RISs promise appealing benefits, their real-world applications still face several major challenges [9]. *Firstly*, the acquisition of channel state information (CSI) is more difficult for RIS-aided networks, since a large number of pilots are required to probe the two-hop source-RIS-destination channels [4]. *Secondly*, the RIS phase shifts have to be optimized together with an active transmit beamformer to enhance the network performance, resulting in high computational complexity [8]. *Thirdly*, the optimized phase shifts have to be sent to the RIS controller over a dedicated feedback link, imposing additional control signaling overhead [7], [10]. The wireless research community is actively working on practical deployments of RISs having scalable overhead and complexity, as detailed in [11]–[13].

A complementary approach to the near-passive RISs is to harness active metasurfaces as transceivers, which are known as large intelligent surfaces (LISs) [14]. Given an electrically large aperture operating in high-frequency bands, the near-field Fresnel region of an LIS may extend to hundreds of meters [15]. The intrinsic spherical wavefront characteristics allow it to reap the full spatial multiplexing gain even under strong LoS propagation conditions [16]. Furthermore, metasurfaces allow for EM operations at an unprecedented level of resolution [17], which underpins the concept of holographic multiple-input and multiple-output (MIMO) communications by modeling an LIS as a near-continuous array of a massive number of infinitesimally small antennas [18]–[21]. In [22], Dardari demonstrated that the effective spatial degrees of freedom (DoFs) offered by holographic MIMO schemes are determined by normalized geometric factors with respect to the wavelength. The unique features of metasurfaces underpin the recent rediscovery of electromagnetic information theory, which aims at *i)* studying and designing physically consistent communication models and wireless transmission schemes, and *ii)* quantifying the maximum amount of information that can be transmitted over a wireless channel, while considering the physical limitations governed by EM laws [23].

Additionally, taking full advantage of wireless propagation environments requires the accurate control of the EM field generated by practical metasurfaces, which, however, have to balance the capability of EM field shaping against the hardware complexity. In this context, the stacked intelligent metasurface (SIM) technology has been proposed for facilitating precise EM control, while implementing some functions, such as MIMO precoding, in the wave domain [24], [25]. Specifically, the computations required are automatically carried out, as the EM waves propagate through an optimized SIM at the speed of light [26]. SIM technology represents a significant reduction in cost, energy usage, and complexity compared to traditional full-digital and hybrid MIMO architectures, while opening up new opportunities for advanced computation relying on EM signal processing [27].

Nevertheless, publicly reported studies on metasurface applications conceived for wireless communications have generally adopted rigid metamaterials [3], [6]. Recently, however, thanks to developments in micro- and nano-fabrication as well as to the discovery of flexible metamaterials, it has become possible to create flexible intelligent metasurfaces (FIMs) by depositing dielectric inclusions onto a conformal flexible substrate [28], [29]. Common flexible substrates with excellent EM and mechanical properties include polyimide, polystyrene, polydimethylsiloxane (PDMS), polyethylene terephthalate (PET), and poly(methyl methacrylate) (PMMA) [30]. Among these, PDMS – a type of silicone polymer – is used most commonly in electronics and optoelectronics due to its low EM losses, ease of fabrication, and favorable elasticity during reversible deformation. Additionally, FIMs can be produced on plastic, elastomeric, and textile substrates [30].

In contrast to rigid metasurfaces, FIMs show significant potential for a wider range of applications, particularly for wave manipulation on conformal and curved surfaces [30]. Potential applications include soft robotics, wearable sensors, invisibility cloaks, artificial smart skin, and implantable devices. Fig. 1 shows some examples of typical FIMs and their applications. In Fig. 1(a), a conformal metasurface is

constructed by embedding silicon disk nanoantennas in a flexible PDMS layer, achieving fine-granularity EM response modification [29]. Fig. 1(b) presents a flexible metaphotonic device consisting of a metallic resonator array on a flexible polyimide substrate, which exhibits an ultrafast switching speed [31]. Fig. 1(c) shows an artificial intelligence-driven invisibility cloaking metasurface capable of rerouting light to conceal objects and adapting to time-varying environments [28], [32]. Inspired by pangolin scales, the authors of [33] fabricated an FIM by periodically mounting rigid EM dissipative scales on a stretchable PDMS substrate, with each scale overlapping its surroundings. As illustrated in Fig. 1(d), this design retains flexible deformation and penetration resistance capabilities. Moreover, Fig. 1(e) shows photonic chip sensor arrays constructed on pliable polymer substrates [34]. These microlaser-based flexible mechanical sensors could detect deformations of flexible chips stimulated by external forces, allowing differentiation of different external types of forces, including the recognition of hand gestures.

While existing FIMs can achieve responsive EM tuning on soft substrates, they cannot support dynamic and programmable morphing between different surface shapes. To address this aspect, the authors of [35] have designed a programmable-shape surface that exploits a liquid metal soft microfluidic network embedded in an elastomer matrix and controlled by EM actuation, which is capable of morphing in real-time with fully reversible capabilities. The liquid-solid phase transition of the liquid metal enables the FIM to fix its surface shape on demand, yet remain reconfigurable. More recently, an FIM was constructed from a matrix of tiny metallic filaments [36], driven by reprogrammable distributed Lorentz forces emanating from electrical currents passing through a static magnetic field[2]. This endows the FIM with precise and rapid dynamic morphing capabilities for promptly changing its structure. Incorporating a mechanical locking construction can hold the newly morphed shapes.

Despite these rich applications, deploying FIMs in wireless networks remains unexplored. In fact, FIMs are particularly well-suited for wireless communications. More specifically, wireless channels generally experience fading effects due to multipath propagation. Multiple copies of the transmitted signal traveling along different paths having different signal attenuations, delays, and phase shifts may result in either constructive or destructive interference at the receiver [37]. However, severe destructive interference can significantly degrade the channel quality, leading to communication outages. Fortunately, strategically optimizing the location of each FIM element may guarantee that the multiple copies of the signal that impinge upon the FIM add constructively to boost the received signal power. This is especially beneficial for wireless networks operating in the mmWave and THz bands [38], since the coherence distance is very small. Therefore, the FIM is expected to be a promising technology for further improving both the spectral and energy efficiency of next-generation wireless networks.

[2]Please refer to https://www.eurekalert.org/multimedia/950133 to watch a video demonstrating the real-time morphing ability of an FIM.

Against this background, we investigate a multiuser multiple-input single-output (MISO) communication system in which an active FIM is deployed at the base station (BS). Specifically, we formulate an optimization problem for minimizing the total transmit power at the BS by jointly optimizing the transmit beamforming vectors and the morphed surface shape of the FIM, subject to specific signal-to-interference-plus-noise ratio (SINR) requirements for each user and the morphing range of the FIM. To solve the formulated problem, we first consider a single-user setting and demonstrate that the optimal surface shape of the FIM is obtained when each element is positioned for maximizing the channel gain. The optimal position is determined using the golden-section search (GSS) technique [39]. However, in multiuser scenarios, the surface shape of the FIM has to cater for the SINR requirements of multiple users, which is a difficult problem to solve optimally due to the non-convex SINR constraints. Therefore, we propose an efficient alternating optimization algorithm for iteratively updating the surface shape of the FIM and the transmit beamforming vectors. In each iteration, the optimal transmit beamforming weights are derived in a closed form given the surface shape of the FIM, while the surface shape of the FIM is updated for increasing the SINR margin and for implicitly reducing the transmit power. Numerical results demonstrate that harnessing an FIM can substantially reduce the transmit power required at the BS to fulfill the SINR targets of the users. Moreover, the analytical and simulation results indicate that the transmit power is reduced logarithmically with the morphing range of the FIM normalized by the radio wavelength.

The remainder of this paper is organized as follows. Section II introduces the system and channel models of an FIM-assisted multiuser MISO system. Section III presents the problem formulated for minimizing the transmit power by optimizing the transmit beamforming weights and the surface shape of the FIM. Section IV introduces the proposed solution and analyzes the performance of the FIM in a single-user scenario, while Section V proposes an efficient alternating optimization algorithm for solving the problem formulated for a multiuser scenario. Section VI presents numerical results to evaluate the performance of the proposed FIM. Finally, Section VII concludes the paper.

*Notation:* Scalars are denoted by italic letters. Vectors and matrices are represented by bold-face lowercase and uppercase letters, respectively; $j = \sqrt{-1}$ denotes the imaginary unit. $|z|$ and $\Im(z)$ denote the absolute value and the imaginary part of a complex number $z$, respectively. For a complex-valued vector $\boldsymbol{v}$, $\|\boldsymbol{v}\|$ denotes its Euclidean norm, and $\mathrm{diag}(\boldsymbol{v})$ produces a diagonal matrix with the elements of $\boldsymbol{v}$ on its main diagonal. For a square matrix $\boldsymbol{S}$, $\boldsymbol{S}^{-1}$ and $(\cdot)^{1/2}$ denote its inverse and square root, respectively. For any general matrix $\boldsymbol{M}$, $\boldsymbol{M}^T$, $\boldsymbol{M}^*$, $\boldsymbol{M}^H$, $\mathrm{rank}(\boldsymbol{M})$, and $[\boldsymbol{M}]_{p,q}$ denote its transpose, conjugate, Hermitian transpose, rank, and the $(p,q)$-th element, respectively. $\boldsymbol{I}_N$ denotes an identity matrix, while $\odot$ represents the Hadamard product. Furthermore, $\mathbb{E}(\cdot)$ stands for the statistical expectation, and $\log(\cdot)$ represents the natural logarithm. $\mathrm{sinc}(x) = \sin(\pi x)/(\pi x)$ is the sinc function. $\mathrm{mod}(x,y)$ returns the remainder from dividing $x$

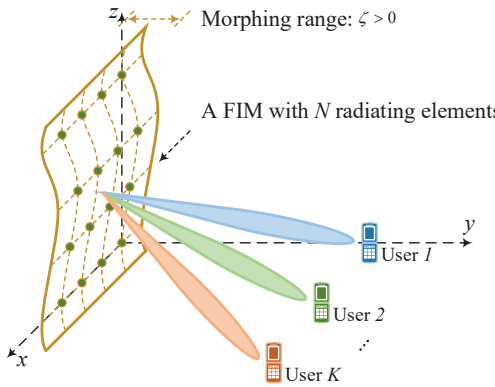


Fig. 2. Schematic of a multiuser MISO system, where an FIM is deployed at the BS.

by $y$. $\lfloor\cdot\rfloor$ and $\lceil\cdot\rceil$ represent the floor and ceiling functions, respectively. The gradient of a scalar function $f$ is denoted by $\nabla f$. $\mathbb{R}$ denotes the set of real numbers, while $\mathbb{C}^n$ and $\mathbb{C}^{x\times y}$ denote the sets of $n$-dimensional complex vectors and of $x \times y$ complex matrices, respectively. The distribution of a circularly symmetric complex Gaussian (CSCG) random vector with mean vector $\boldsymbol{x}$ and covariance matrix $\boldsymbol{\Sigma}$ is denoted by $\sim \mathcal{CN}(\boldsymbol{x}, \boldsymbol{\Sigma})$, where $\sim$ means "distributed as". $\mathcal{U}(x, y)$ represents the uniform distribution over the interval $(x, y)$.

## II. System, Channel and Signal Models

### A. System Model

As shown in Fig. 2, we consider the downlink of a multiuser MISO communication system operating in a single cell, where a BS equipped with an FIM communicates simultaneously with $K$ single-antenna mobile users. The FIM antenna array is modeled as a uniform planar array (UPA) located on the $x$-$z$ plane. Let $N = N_x N_z \geq K$ represent the total number of transmit antennas, with $N_x$ and $N_z$ referring to the number of antenna elements along the $x$-axis and $z$-axis, respectively. We define the sets of antennas and users as $\mathcal{N} \triangleq \{1, 2, \cdots, N\}$ and $\mathcal{K} \triangleq \{1, 2, \cdots, K\}$, respectively.

In contrast to conventional communication systems relying on rigid antenna arrays, each radiating element of the FIM can be flexibly positioned along the direction perpendicular to the surface, i.e., the $y$-axis, with the aid of a controller. Specifically, let $\boldsymbol{p}_n = [x_n, y_n, z_n]^T \in \mathbb{R}^3,\ \forall n \in \mathcal{N}$ represent the location of the $n$-th radiating element[3]. Taking the first element as a reference point, we have

$$x_n = d_x \times \mathrm{mod}\,(n-1, N_x)\,, \tag{1}$$

$$z_n = d_z \times \lfloor (n-1)/N_x \rfloor\,, \tag{2}$$

for $\forall n \in \mathcal{N}$, where $d_x$ and $d_z$ denote the spacing between adjacent antenna elements in the $x$- and $z$-directions, respectively. Furthermore, the $y$-coordinate of each radiating element can be adjusted within the maximum range allowed by the reversible deformation of the FIM [36], satisfying

$$y_{\min} \leq y_n \leq y_{\max}, \quad \forall n \in \mathcal{N}, \tag{3}$$

where $y_{\min}$ and $y_{\max}$ represent the minimum and maximum $y$-coordinates of each element, and $\zeta = y_{\max} - y_{\min} > 0$ is termed as the *morphing range* characterizing the range of reversible deformation. We set $y_{\min} = 0$ throughout this paper.

As a result, the surface shape of the FIM is characterized by

$$\text{FIM's surface shape:} \quad \boldsymbol{y} = [y_1, y_2, \cdots, y_N]^T \in \mathbb{C}^N. \tag{4}$$

***Remark** 1:* Note that placing the UPA on the $x$-$z$ plane is an arbitrary choice made for notational simplicity. All the algorithms and conclusions discussed in this paper apply regardless of the array orientation.

### B. Multipath Channel Model

Moreover, we assume that all channels experience quasi-static flat fading. Let $\boldsymbol{h}_k^H \in \mathbb{C}^{1\times N},\ \forall k \in \mathcal{K}$ denote the baseband equivalent channel spanning from the FIM at the BS to the $k$-th user's receiver antenna. We adopt the multipath channel representation of [40] to characterize the wireless channels. Specifically, the channel $\boldsymbol{h}_k^H$ is modeled as a composite response of multiple propagation paths.

For a scatterer in the far field of the FIM, the phase profile observed by the antenna array depends on the scattering elevation angle $\theta \in [0, \pi)$, azimuth angle $\phi \in [0, \pi)$, and the FIM's surface-shape vector $\boldsymbol{y}$. Specifically, the array steering vector $\boldsymbol{a}(\boldsymbol{y}, \phi, \theta)$ is given by

$$\boldsymbol{a}(\boldsymbol{y}, \phi, \theta) = \Big[1, \cdots, e^{j\kappa(x_n \sin\theta\cos\phi + y_n \sin\theta\sin\phi + z_n\cos\theta)}, \cdots, e^{j\kappa(x_N \sin\theta\cos\phi + y_N \sin\theta\sin\phi + z_N\cos\theta)}\Big]^T, \tag{5}$$

where $\kappa = 2\pi/\lambda$ represents the wavenumber, with $\lambda$ denoting the carrier's wavelength.

Furthermore, let $L$ represent the number of propagation paths between each user and the BS, while the corresponding path set is defined by $\mathcal{L} \triangleq \{1, 2, \cdots, L\}$. The complex gain of the $\ell$-th propagation path spanning from the $k$-th user to the BS is represented by $\alpha_{k,\ell} \in \mathbb{C},\ \forall \ell \in \mathcal{L},\ \forall k \in \mathcal{K}$, while $\theta_\ell$ and $\phi_\ell$ are the elevation and azimuth angles of arrival (AoA), respectively, for the $\ell$-th propagation path. As a result, the narrowband channel $\boldsymbol{h}_k$ can be written as

$$\boldsymbol{h}_k(\boldsymbol{y}) = \sum_{\ell=1}^{L} \alpha_{k,\ell} \boldsymbol{a}(\boldsymbol{y}, \phi_\ell, \theta_\ell)\,, \quad \forall k \in \mathcal{K}. \tag{6}$$

In this paper, we assume that $\alpha_{k,\ell},\ \forall \ell \in \mathcal{L},\ \forall k \in \mathcal{K}$ are independent and identically distributed (i.i.d.) CSCG variables, satisfying $\alpha_{k,\ell} \sim \mathcal{CN}\left(0, \rho_{k,\ell}^2\right)$, where $\rho_{k,\ell}^2$ represents the average power of the $\ell$-th path associated with the $k$-th user [40]. Furthermore, let $\beta_k$ characterize the path loss between the $k$-th user and the BS. Thus, we have $\sum_{\ell=1}^{L} \rho_{k,\ell}^2 = \beta_k,\ \forall k \in \mathcal{K}$.

***Remark** 2:* We adopt a time-division duplexing (TDD) protocol for uplink and downlink transmissions. Channel reciprocity is utilized for the CSI acquisition in the downlink

[3]In this paper, we focus on morphing the surface shape of the FIM, with each element on the FIM abstracted as a point for simplicity. The examination of real-world aperture losses caused by stretching the FIM is left for future research.

based on the uplink channel training. To characterize the theoretical performance gain of the FIM, we assume that both the BS and users have perfect knowledge of the CSI, which can be obtained by probing channels associated with predesigned surface shapes and employing appropriate interpolation techniques. Moreover, advanced techniques, such as the compressed sensing and the space-alternating generalized expectation maximization algorithm can be utilized to estimate channels in FIM-assisted wireless systems at a moderate overhead [41].

### C. Signal Model

Space division multiple access (SDMA) is utilized for separating the $K$ different data signals spatially for serving multiple users simultaneously over the same time/frequency resource block [37]. The BS employs a linear transmit precoding strategy to send signals from $N$ antennas to multiple users [42]. Let $s_k \in \mathbb{C},\ k \in \mathcal{K}$ denote the normalized information signal for user $k$, which are assumed to be independent random variables with zero mean and unit variance. Additionally, $\boldsymbol{w}_k \in \mathbb{C}^N$ represents the dedicated beamforming vector assigned to user $k$, and $P_{\mathrm{t}} = \sum_{k=1}^{K} \|\boldsymbol{w}_k\|^2$ denotes the transmit power of the BS. Therefore, the complex baseband signal $\boldsymbol{u} \in \mathbb{C}^N$ transmitted from the BS can be expressed as

$$\boldsymbol{u} = \sum_{k=1}^{K} \boldsymbol{w}_k s_k. \tag{7}$$

After passing through the wireless channel, the complex baseband signal $r_k \in \mathbb{C},\ \forall k \in \mathcal{K}$ received at user $k$ is expressed as

$$\begin{aligned} r_k &= \boldsymbol{h}_k^H(\boldsymbol{y})\,\boldsymbol{u} + n_k = \boldsymbol{h}_k^H(\boldsymbol{y}) \sum_{k'=1}^{K} \boldsymbol{w}_{k'} s_{k'} + n_k \\ &= \underbrace{\boldsymbol{h}_k^H(\boldsymbol{y})\,\boldsymbol{w}_k s_k}_{\text{Intended Signal}} + \underbrace{\boldsymbol{h}_k^H(\boldsymbol{y}) \sum_{k'=1,\,k'\neq k}^{K} \boldsymbol{w}_{k'} s_{k'}}_{\text{Interference}} + \underbrace{n_k}_{\text{Noise}}, \end{aligned} \tag{8}$$

where $n_k \sim \mathcal{CN}\left(0, \sigma_k^2\right)$ represents the additive white Gaussian noise (AWGN) at user $k$'s receiver, with $\sigma_k^2$ being the corresponding noise power.

Accordingly, the SINR experienced by user $k$ can be determined as

$$\mathrm{SINR}_k = \frac{\left|\boldsymbol{h}_k^H(\boldsymbol{y})\,\boldsymbol{w}_k\right|^2}{\sum\limits_{k'=1,\ k'\neq k}^{K} \left|\boldsymbol{h}_k^H(\boldsymbol{y})\,\boldsymbol{w}_{k'}\right|^2 + \sigma_k^2}, \quad \forall k \in \mathcal{K}. \tag{9}$$

***Remark 3:*** Conventionally, the multiuser transmit beamformer has to strike tradeoffs between boosting the signal power for the intended user, while reducing the interference for others. On the other hand, the FIM provides extra design DoFs to meet the QoS requirements in a more energy-efficient way. The surface shape of the FIM can be morphed so that the desired signal components add constructively at the intended user, while combining destructively at unintended users.

***Remark 4:*** Note that the surface shape of the FIM is only updated at each new channel coherence block, which occurs on a much longer timescale than the symbol duration. With advanced EM actuation technology, it is possible to achieve dynamic surface-shape morphing in just a few milliseconds [36]. Moreover, for rapidly time-varying channels with shorter coherence time, one may consider to optimize the ergodic performance over multiple coherence blocks or design suboptimal methods for morphing the surface shape of the FIM to strike tradeoffs between the achievable performance and implementation complexity.

## III. Power Minimization Problem Formulation

In this section, we aim for minimizing the total transmit power at the BS by jointly optimizing the transmit beamforming vectors $\{\boldsymbol{w}_k\}$ associated with multiple users and the surface shape $\boldsymbol{y}$ of the FIM, subject to a set of individual SINR requirements for the $K$ users and the morphing range. Specifically, the joint optimization problem is formulated as

$$(P_{\mathcal{A}}) \quad \min_{\{\boldsymbol{w}_k\},\,\boldsymbol{y}} \quad \sum_{k=1}^{K} \|\boldsymbol{w}_k\|^2 \tag{10a}$$

$$\text{s.t.} \quad \frac{\left|\boldsymbol{h}_k^H(\boldsymbol{y})\,\boldsymbol{w}_k\right|^2}{\sum\limits_{k'\neq k}^{K} \left|\boldsymbol{h}_k^H(\boldsymbol{y})\,\boldsymbol{w}_{k'}\right|^2 + \sigma_k^2} \geq \gamma_k, \quad \forall k \in \mathcal{K}, \tag{10b}$$

$$0 \leq y_n \leq y_{\max}, \quad \forall n \in \mathcal{N}, \tag{10c}$$

where $\gamma_k > 0$ represents the minimum SINR requirement for user $k$ to achieve its desired data rate.

While the objective function of $(P_{\mathcal{A}})$ and the constraints in (10c) are convex, problem $(P_{\mathcal{A}})$ is challenging to solve optimally due to the non-convex constraint in (10b) [8], [42]. Additionally, the transmit beamforming vectors and the FIM's surface shape are highly coupled. In the next section, we first solve $(P_{\mathcal{A}})$ for the single-user case, which is then generalized to the multiuser scenario in Section V.

## IV. Single-User Scenario

In this section, we aim for gleaning fundamental insights into designing the optimal surface shape of the FIM for $K = 1$. In this case, problem $(P_{\mathcal{A}})$ is simplified to

$$(P_{\mathcal{B}}) \quad \min_{\boldsymbol{w},\,\boldsymbol{y}} \quad \|\boldsymbol{w}\|^2 \tag{11a}$$

$$\text{s.t.} \quad \left|\boldsymbol{h}^H(\boldsymbol{y})\,\boldsymbol{w}\right|^2 \geq \gamma\sigma^2, \tag{11b}$$

$$0 \leq y_n \leq y_{\max}, \quad \forall n \in \mathcal{N}, \tag{11c}$$

where the user index subscript has been omitted for the sake of brevity. Nevertheless, problem $(P_{\mathcal{B}})$ remains non-convex, since the left-hand-side of (11b) is not jointly concave with respect to $\boldsymbol{h}(\boldsymbol{y})$ and $\boldsymbol{w}$. Next, we will decompose problem $(P_{\mathcal{B}})$ into two subproblems and solve them efficiently.

### A. Optimal Transmit Beamforming – MRT

Given the surface shape of the FIM $\boldsymbol{y}$, the optimal transmit beamforming vector $\boldsymbol{w}$ of problem $(P_{\mathcal{B}})$ is the one that maximizes the signal power received by the intended user. This yields the well-known maximal ratio transmission (MRT) beamforming along the same direction as the channel [37], i.e.,

$$\boldsymbol{w}^{\mathrm{o}} = \sqrt{P_{\mathrm{t}}}\frac{\boldsymbol{h}\left(\boldsymbol{y}\right)}{\left\|\boldsymbol{h}\left(\boldsymbol{y}\right)\right\|}. \tag{12}$$

### B. Surface-Shape Morphing – Golden-Section Search

Substituting the optimal beamforming vector $\boldsymbol{w}^{\mathrm{o}}$ into problem $(P_{\mathcal{B}})$ yields the following simplified problem:

$$\begin{aligned}(P_{\mathcal{C}}) \quad \min_{\boldsymbol{y}} \quad & P_{\mathrm{t}} && \text{(13a)}\\ \text{s.t.} \quad & P_{\mathrm{t}}\left\|\boldsymbol{h}\left(\boldsymbol{y}\right)\right\|^2 \geq \gamma\sigma^2, && \text{(13b)}\\ & 0 \leq y_n \leq y_{\max}, \quad \forall n \in \mathcal{N}. && \text{(13c)}\end{aligned}$$

It is easy to verify that the optimal transmit power of problem $(P_{\mathcal{C}})$ is $P_{\mathrm{t}}^{\mathrm{o}} = \gamma\sigma^2/\left\|\boldsymbol{h}\left(\boldsymbol{y}\right)\right\|^2$. As a result, minimizing the transmit power is equivalent to maximizing the channel gain, and the original problem is reduced to

$$\begin{aligned}(P_{\mathcal{D}}) \quad \max_{\boldsymbol{y}} \quad & \left\|\boldsymbol{h}\left(\boldsymbol{y}\right)\right\|^2 && \text{(14a)}\\ \text{s.t.} \quad & 0 \leq y_n \leq y_{\max}, \quad \forall n \in \mathcal{N}. && \text{(14b)}\end{aligned}$$

Note that, for the single-user scenario, the surface-shape morphing can be decoupled into the position optimization of $N$ individual elements due to the fact that $\left\|\boldsymbol{h}\left(\boldsymbol{y}\right)\right\|^2 = \sum_{n=1}^{N}\left|h_n\left(y_n\right)\right|^2$. More explicitly, each term in the objective function depends only on the position of the corresponding element. This means that solving problem $(P_{\mathcal{D}})$ is equivalent to solving $N$ separate subproblems as follows:

$$\begin{aligned}(P_{\mathcal{E}}) \quad \max_{y_n} \quad & \left|h_n\left(y_n\right)\right|^2 && \text{(15a)}\\ \text{s.t.} \quad & 0 \leq y_n \leq y_{\max}. && \text{(15b)}\end{aligned}$$

Note that the original problem has now been simplified to a single variable optimization problem with respect to the position $y_n$ of the $n$-th element, which can be readily solved by applying a standard line search method. Additionally, it is demonstrated that, in a single-user scenario, each FIM element should be positioned to have the highest channel gain.

Furthermore, the GSS approach combined with appropriate exploration techniques [39] can be utilized for further reducing the search complexity[4]. To address the issue that the GSS might only find a local maximum of the objective function $\left|h_n\left(y_n\right)\right|^2$, we divide the interval $[0, y_{\max}]$ into multiple smaller regions and apply the GSS in each segment. Specifically, assuming that the interval is divided into $M$ segments: $0 = y_{n,0} < y_{n,1} < \cdots < y_{n,M} = y_{\max}$, and let $y_{n,m}^{\mathrm{o}},\ m = 1, 2, \cdots, M$ denote the local maximum point obtained by applying the GSS in the $m$-th segment. As a result, the optimal position for the $n$-th element is determined by

$$y_n^{\mathrm{o}} = \arg\max_{y_n \in \mathcal{G}_n}\left|h_n\left(y_n\right)\right|^2, \tag{16}$$

where $\mathcal{G}_n \triangleq \left\{y_{n,0}, y_{n,1}^{\mathrm{o}}, y_{n,1}, y_{n,2}^{\mathrm{o}}, y_{n,2}, \cdots, y_{n,M}^{\mathrm{o}}, y_{n,M}\right\}$ represents the set that collects the endpoints and local maximum points of all segments. Note that the end points of each segment are also included in $\mathcal{G}_n$, since the GSS approach only evaluates the function at the interior points in each segment.

Solving problem $(P_{\mathcal{E}})$ for all $N$ elements results in the optimal surface shape of the FIM $\boldsymbol{y}^{\mathrm{o}} = [y_1^{\mathrm{o}}, y_2^{\mathrm{o}}, \cdots, y_N^{\mathrm{o}}]^T$.

***Remark** 5:* The convexity of $\left|h_n\left(y_n\right)\right|^2$ can be asymptotically guaranteed by appropriately increasing the number of segments in the interval $0 \leq y_n \leq y_{\max}$, thus ensuring that the solution in (16) is globally optimal. For instance, when considering a single scatterer, $\left|h_n\left(y_n\right)\right|^2$ is a periodic function with period $\lambda/\left(\sin\theta\sin\phi\right)$. In this case, taking $M = \lceil \kappa y_{\max}\sin\theta\sin\phi/\pi \rceil$ is adequate. When considering rich scattering environments, the value of $M$ may have to be increased linearly with the number of scatterers.

### C. Performance Analysis

Next, we examine the performance gain attained by the FIM by deriving the scaling law of the average power $P_{\mathrm{r}}$ received at the user with respect to the maximum morphing range $y_{\max}$. In order to obtain essential insights, we make some reasonable assumptions for simplifying the analysis and explain their effects.

- We assume that the number of scatterers approaches infinity, i.e., $L \to \infty$. According to the Lindeberg-Lévy central limit theorem, the channel coefficient becomes a random variable satisfying $h_n\left(y_n\right) \sim \mathcal{CN}\left(0, \beta^2\right)$ and $\mathbb{E}\left(\left|h_n\left(y_n\right)\right|^2\right) = \beta^2$, which means that the channel experiences Rayleigh fading.
- We assume an isotropic channel environment, so the spatial correlation between an arbitrary pair of spatial points for an antenna element is characterized by $r_{m,m'} = \mathrm{sinc}\left(\kappa d_{m,m'}/\pi\right)$ [19], where $d_{m,m'}$ is the corresponding distance.
- We assume the statistical independence between arbitrary pairs of antenna elements. This can be achieved by considering half-wavelength element spacing, i.e., $d_x = d_z = \lambda/2$[5].

Specifically, the average power received by the user is given by

$$P_{\mathrm{r}} = P_{\mathrm{t}}\mathbb{E}\left(\left\|\boldsymbol{h}\left(\boldsymbol{y}\right)\right\|^2\right) = P_{\mathrm{t}}\sum_{n=1}^{N}\mathbb{E}\left(\left|h_n\left(y_n\right)\right|^2\right). \tag{17}$$

When a rigid antenna array (i.e., $y_n = 0$), or an FIM having a random surface shape (i.e., $y_n \sim \mathcal{U}\left[0, y_{\max}\right]$) is used, the average received power is given by $P_{\mathrm{r}} = P_{\mathrm{t}}N\beta^2$, which increases linearly with $N$. By contrast, the average received power of the optimal FIM surface shape is summarized in *Proposition 1*.

[4]In MATLAB, the GSS approach has been encapsulated into a built-in function – *fminbnd*.

[5]Note that the statistical independence cannot be strictly satisfied for a UPA. However, as the element spacing increases, the correlation between the elements becomes negligible. In order to characterize the effects of $\zeta$ on system performance, we assume i.i.d. channels across different elements, which is a reasonable approximation in many situations.

TABLE I
TYPICAL VALUES OF $\Delta(\zeta)$ WITH RESPECT TO $\zeta$.

| $\zeta$ | 0 | $\lambda/2$ | $\lambda$ | $3\lambda/2$ | $2\lambda$ | $5\lambda/2$ | $3\lambda$ | $7\lambda/2$ | $4\lambda$ |
|---|---|---|---|---|---|---|---|---|---|
| $\Delta(\zeta)$ | 0.43 | 0.48 | 0.50 | 0.53 | 0.55 | 0.60 | 0.60 | 0.62 | 0.63 |

*Proposition 1:* For the optimal FIM surface shape $\boldsymbol{y}^{\mathrm{o}} = [y_1^{\mathrm{o}}, y_2^{\mathrm{o}} \cdots, y_N^{\mathrm{o}}]^T$, the average power received by the user is given by

$$P_{\mathrm{r}} \simeq P_{\mathrm{t}} N \beta^2 \left[\log\left(\kappa\zeta/\pi + 1\right) + C + \Delta\left(\zeta\right)\right], \tag{18}$$

where $C \approx 0.57722$ is the Euler-Mascheroni constant, while $\Delta(\zeta)$ characterizes the gap between the numerical and the analytical results. Typical values of $\Delta(\zeta)$ with respect to the morphing range $\zeta$ are listed in Table I.

*Proof:* Please refer to Appendix A.

The logarithmic power scaling law in *Proposition 1* indicates that the transmit power of the BS can be scaled down by a factor of $1/\log(\kappa\zeta/\pi)$ for the optimal FIM surface shape, without compromising the user's received signal power. This is due to the fact that the FIM provides an inherent *selection gain* by strategically placing each element at the position of the strongest channel gain [37]. Additionally, *Proposition 1* also characterizes the maximum power gain that an FIM can offer in practical scenarios with a limited number of scatterers.

## V. MULTIUSER SCENARIO

In this section, we characterize FIM-assisted multiuser MISO communications. Since the joint optimization problem $(P_{\mathcal{A}})$ is quite challenging to solve optimally, we propose an efficient alternating optimization algorithm and derive the asymptotic beamforming vectors in the high signal-to-noise ratio (SNR) region.

### A. The Proposed Alternating Optimization Algorithm

The alternating optimization algorithm involves solving a pair of subproblems. Specifically, the transmit beamforming vectors and the FIM's surface shape are optimized iteratively in an alternating fashion, until convergence is reached.

*1) Transmit Beamforming Optimization $\{\boldsymbol{w}_k\}$ Given the FIM's Surface Shape $\hat{\boldsymbol{y}}$:* For a tentative surface-shape vector $\hat{\boldsymbol{y}}$, the wireless channel spanning from user $k$ to the BS is determined by $\boldsymbol{h}_k(\hat{\boldsymbol{y}}) = \sum_{\ell=1}^{L} \alpha_{k,\ell} \boldsymbol{a}(\hat{\boldsymbol{y}}, \phi_\ell, \theta_\ell)$, $\forall k \in \mathcal{K}$. Thus, the original problem $(P_{\mathcal{A}})$ is reduced to only optimizing the transmit beamforming vectors, i.e.,

$$(P_{\mathcal{F}}) \quad \min_{\{\boldsymbol{w}_k\}} \quad \sum_{k=1}^{K} \|\boldsymbol{w}_k\|^2 \tag{19a}$$

$$\text{s.t.} \quad \frac{\left|\boldsymbol{h}_k^H(\hat{\boldsymbol{y}})\,\boldsymbol{w}_k\right|^2}{\sum\limits_{k' \neq k}^{K} \left|\boldsymbol{h}_k^H(\hat{\boldsymbol{y}})\,\boldsymbol{w}_{k'}\right|^2 + \sigma_k^2} \geq \gamma_k, \quad \forall k \in \mathcal{K}. \tag{19b}$$

Note that problem $(P_{\mathcal{F}})$ is the conventional power minimization problem in the multiuser MISO downlink broadcast channel, which can be efficiently solved by utilizing a fixed-point iterative algorithm based on uplink-downlink duality [43], [44]. It has been shown that Slater's constraint qualification is fulfilled [42], which implies that strong duality holds and the Karush–Kuhn–Tucker (KKT) conditions are necessary and sufficient for determining the optimal solution.

By leveraging the stationarity of KKT conditions at the optimal solution [42], the optimal minimum mean square error (MMSE) beamforming vectors $\boldsymbol{w}_k^{\mathrm{o}}$, $\forall k \in \mathcal{K}$ have the following general form

$$\boldsymbol{w}_k^{\mathrm{o}} = \sqrt{p_k} \underbrace{\frac{\left(\boldsymbol{I}_N + \sum\limits_{k'=1}^{K} \frac{\lambda_{k'}}{\sigma_{k'}^2} \boldsymbol{h}_{k'}(\hat{\boldsymbol{y}})\,\boldsymbol{h}_{k'}^H(\hat{\boldsymbol{y}})\right)^{-1} \boldsymbol{h}_k(\hat{\boldsymbol{y}})}{\left\|\left(\boldsymbol{I}_N + \sum\limits_{k'=1}^{K} \frac{\lambda_{k'}}{\sigma_{k'}^2} \boldsymbol{h}_{k'}(\hat{\boldsymbol{y}})\,\boldsymbol{h}_{k'}^H(\hat{\boldsymbol{y}})\right)^{-1} \boldsymbol{h}_k(\hat{\boldsymbol{y}})\right\|}}_{=\tilde{\boldsymbol{w}}_k^{\mathrm{o}},\ \text{transmit beamforming direction}}, \tag{20}$$

where $\lambda_k \geq 0$ is the Lagrange multiplier associated with the $k$-th SINR constraint, while $p_k$ denotes the corresponding beamforming power. It can be readily proved by the method of contradiction that the SINR constraints in (19b) are met with equality at the optimal solution [45]. As a consequence, solving the $K$ linear equations in (19b) yields the solutions of the $K$ unknown beamforming powers $p_k$ as

$$[p_1, p_2, \cdots, p_K]^T = \boldsymbol{M}^{-1} \left[\sigma_1^2, \sigma_2^2, \cdots, \sigma_K^2\right]^T, \tag{21}$$

where the $(k, k')$-th element of the matrix $\boldsymbol{M} \in \mathbb{R}^{K \times K}$ is given by

$$[\boldsymbol{M}]_{k,k'} = \begin{cases} \frac{1}{\gamma_k} \left|\boldsymbol{h}_k^H(\hat{\boldsymbol{y}})\,\tilde{\boldsymbol{w}}_k^{\mathrm{o}}\right|^2, & k = k', \\ -\left|\boldsymbol{h}_k^H(\hat{\boldsymbol{y}})\,\tilde{\boldsymbol{w}}_{k'}^{\mathrm{o}}\right|^2, & k \neq k'. \end{cases} \tag{22}$$

By combining (20) and (21), we can express the structure of the optimal beamforming vectors in terms of the Lagrange multipliers $\lambda_1, \lambda_2, \cdots, \lambda_K$. Leveraging the property of strong duality, the Lagrange multipliers can be calculated using convex optimization techniques [43] or by iteratively solving the fixed-point equations shown in (23) [44].

*2) Surface-Shape Morphing $\boldsymbol{y}$ Given the Beamforming Vectors $\{\hat{\boldsymbol{w}}_k\}$:* Next, we consider morphing the FIM's surface shape $\boldsymbol{y}$, given the calculated transmit beamforming vectors $\hat{\boldsymbol{w}}_1, \hat{\boldsymbol{w}}_2, \cdots, \hat{\boldsymbol{w}}_K$ in (20). In this case, problem $(P_{\mathcal{A}})$ is reduced to a feasibility-check problem with respect to the

$$\lambda_k = \frac{\gamma_k \sigma_k^2}{(\gamma_k+1)\,\boldsymbol{h}_k^H(\hat{\boldsymbol{y}})\left(\boldsymbol{I}_N + \sum_{k'=1}^K \frac{\lambda_{k'}}{\sigma_{k'}^2}\boldsymbol{h}_{k'}(\hat{\boldsymbol{y}})\,\boldsymbol{h}_{k'}^H(\hat{\boldsymbol{y}})\right)^{-1}\boldsymbol{h}_k(\hat{\boldsymbol{y}})}, \quad \forall k \in \mathcal{K}. \tag{23}$$

FIM's surface shape, which can be formulated as

$$(P_{\mathcal{G}}) \quad \text{Find} \quad \boldsymbol{y} \tag{24a}$$

$$\text{s.t.} \quad \frac{\left|\boldsymbol{h}_k^H(\boldsymbol{y})\,\hat{\boldsymbol{w}}_k\right|^2}{\sum_{k'\neq k}^K \left|\boldsymbol{h}_k^H(\boldsymbol{y})\,\hat{\boldsymbol{w}}_{k'}\right|^2 + \sigma_k^2} \geq \gamma_k, \quad \forall k \in \mathcal{K}, \tag{24b}$$

$$0 \leq y_n \leq y_{\max}, \quad \forall n \in \mathcal{N}. \tag{24c}$$

In order to obtain an efficient solution for the FIM's surface shape, we transform problem $(P_{\mathcal{G}})$ into an optimization problem with an explicit objective function. The rationale underlying this approach is that, in the transmit beamforming optimization problem $(P_{\mathcal{F}})$, all the SINR constraints will be met with equality at the optimal solution [42]. Therefore, morphing the surface shape to enforce the achievable SINR for each user to be larger than the corresponding SINR target in $(P_{\mathcal{G}})$ implicitly leads to a lower transmit power value in $(P_{\mathcal{F}})$. To this end, we define a slack variable $\epsilon_k$ to characterize the residual SINR margin for user $k$, i.e.,

$$\epsilon_k \triangleq \frac{1}{\gamma_k \sigma_k^2}\left|\boldsymbol{h}_k^H(\boldsymbol{y})\,\hat{\boldsymbol{w}}_k\right|^2 - \frac{1}{\sigma_k^2}\sum_{k'\neq k}^K \left|\boldsymbol{h}_k^H(\boldsymbol{y})\,\hat{\boldsymbol{w}}_{k'}\right|^2 - 1, \tag{25}$$

which satisfies $\epsilon_k \geq 0,\ \forall k \in \mathcal{K}$.

By introducing the auxiliary variable $\epsilon_k$, $(P_{\mathcal{G}})$ is transformed into

$$(P_{\mathcal{H}}) \quad \max_{\boldsymbol{y}} \quad \epsilon = \sum_{k=1}^K \epsilon_k \tag{26a}$$

$$\text{s.t.} \quad 0 \leq y_n \leq y_{\max}, \quad \forall n \in \mathcal{N}, \tag{26b}$$

$$\epsilon_k \geq 0, \quad \forall k \in \mathcal{K}, \tag{26c}$$

which can be efficiently solved by applying the gradient ascent method. Specifically, given the surface shape of the FIM found from the last iteration as the initial point, we adapt it towards the direction of the gradient for gradually increasing the objective function value $\epsilon$.

According to (25), the gradient of $\epsilon$ with respect to $\boldsymbol{y}$ is given by

$$\nabla_{\boldsymbol{y}}\epsilon = \sum_{k=1}^K \frac{1}{\gamma_k\sigma_k^2}\nabla_{\boldsymbol{y}}\left|\boldsymbol{h}_k^H(\boldsymbol{y})\,\hat{\boldsymbol{w}}_k\right|^2 - \sum_{k=1}^K \frac{1}{\sigma_k^2}\sum_{k'\neq k}^K \nabla_{\boldsymbol{y}}\left|\boldsymbol{h}_k^H(\boldsymbol{y})\,\hat{\boldsymbol{w}}_{k'}\right|^2. \tag{27}$$

Note that the gradient $\nabla_{\boldsymbol{y}}\epsilon$ in (27) depends on the general term $\nabla_{\boldsymbol{y}}\left|\boldsymbol{h}_k^H(\boldsymbol{y})\,\hat{\boldsymbol{w}}_{k'}\right|^2,\ \forall k,k' \in \mathcal{K}$, which can be calculated as [46]

$$\nabla_{\boldsymbol{y}}\left|\boldsymbol{h}_k^H(\boldsymbol{y})\,\hat{\boldsymbol{w}}_{k'}\right|^2 = -2\kappa\sum_{\ell=1}^L \sin\theta_\ell \sin\phi_\ell \times \Im\left\{\alpha_{k,\ell}\left(\boldsymbol{a}(\boldsymbol{y},\phi_\ell,\theta_\ell)\odot\hat{\boldsymbol{w}}_{k'}^*\right)\boldsymbol{h}_k^H(\boldsymbol{y})\,\hat{\boldsymbol{w}}_{k'}\right\}. \tag{28}$$

Substituting (28) into (27) results in the explicit expression of the gradient $\nabla_{\boldsymbol{y}}\epsilon$, which is omitted here for brevity.

Therefore, at each iteration, the surface shape of the FIM is updated by

$$\boldsymbol{y} \leftarrow \boldsymbol{y} + \mu\nabla_{\boldsymbol{y}}\epsilon, \tag{29}$$

where $\mu > 0$ represents the step size, which is determined by applying the backtracking line search.

Additionally, a projection process is imposed on each position obtained in (29) for scaling it into the effective morphing range of the FIM, yielding

$$y_n = \max\left(\min\left(y_n, y_{\max}\right), 0\right), \quad \forall n \in \mathcal{N}. \tag{30}$$

***Remark** 6:* Note that the surface-shape update in (29) may not guarantee an increase in the SINR margin for all the users, especially for a large number of users. To address this issue, we slightly relax the condition in (26c) by introducing a variable $\epsilon_{\min} < 0$ and add a power discrimination step for ensuring that the relaxed SINR constraint still results in power reduction. Specifically, at the $i$-th iteration, two conditions have to be satisfied, when applying the backtracking line search: *i)* $\epsilon_k^{(i)} \geq \epsilon_{\min},\ \forall k \in \mathcal{K}$, and *ii)* $P_{\mathrm{t}}^{(i)} \leq P_{\mathrm{t}}^{(i-1)}$. Note that the constraint in (24b) is not violated since it is strictly satisfied with equality after solving subproblem $(P_{\mathcal{F}})$ in the next iteration [43]. Additionally, one may strategically increase the threshold $\epsilon_{\min}$ to guarantee that the relaxation is asymptotically tight.

In a nutshell, the proposed alternating optimization algorithm solves problem $(P_{\mathcal{A}})$ by alternately solving the subproblems $(P_{\mathcal{F}})$ and $(P_{\mathcal{H}})$ in an iterative manner. The details of the alternating optimization algorithm are outlined in Algorithm 1 and its convergence is guaranteed for two reasons: *i)* the solution for each subproblem ensures that the objective function value of $(P_{\mathcal{A}})$ is non-increasing over consecutive iterations, and *ii)* the objective function value of $(P_{\mathcal{A}})$ is lower bounded due to the SINR constraints in (10b). Additionally, we strategically conclude the alternating optimization algorithm by a final transmit beamforming optimization due to the relaxation when solving $(P_{\mathcal{G}})$.

### *B. Low-Complexity Transmit Beamforming Optimization – ZF*

Next, we simplify the transmit beamforming by examining its asymptotically optimal version – namely zero-forcing

**Algorithm 1** The Proposed Alternating Optimization Algorithm.

1: **Input**: $\alpha_{k,\ell},\ \phi_\ell,\ \theta_\ell,\ \forall \ell \in \mathcal{L},\ \gamma_k,\ \sigma_k^2,\ \forall k \in \mathcal{K},\ y_{\max}$.
2: Initialize the surface shape $\boldsymbol{y}^{(0)}$ and set the iteration counter to $i = 0$.
3: **Repeat**
4: Solve problem $(P_{\mathcal{F}})$ for the given $\boldsymbol{y}^{(i)}$, and denote the optimal transmit beamforming vector as $\left\{\boldsymbol{w}_k^{(i)}\right\}$.
5: Solve problem $(P_{\mathcal{H}})$ for the given $\left\{\boldsymbol{w}_k^{(i)}\right\}$, and denote the optimal surface shape of the FIM as $\boldsymbol{y}^{(i+1)}$.
6: Increase the iteration counter by $i \leftarrow i+1$.
7: **Until** The fractional decrease of the transmit power $P_{\mathrm{t}}$ falls below a preset threshold or $i$ exceeds the maximum tolerable number of iterations.
8: **Output**: $\boldsymbol{w}_1^{\mathrm{o}},\ \boldsymbol{w}_2^{\mathrm{o}},\ \cdots,\ \boldsymbol{w}_K^{\mathrm{o}},\ \boldsymbol{y}^{\mathrm{o}}$.

(ZF) beamforming – in the high-SNR region. Let us define $\boldsymbol{W} \triangleq [\boldsymbol{w}_1, \boldsymbol{w}_2, \cdots, \boldsymbol{w}_K] \in \mathbb{C}^{N\times K}$, and $\boldsymbol{H}(\boldsymbol{y}) \triangleq [\boldsymbol{h}_1(\boldsymbol{y}), \boldsymbol{h}_2(\boldsymbol{y}), \cdots, \boldsymbol{h}_K(\boldsymbol{y})] \in \mathbb{C}^{N\times K}$. The ZF beamformer is given by

$$\boldsymbol{W}_{\mathrm{ZF}} = \boldsymbol{H}(\boldsymbol{y}) \left(\boldsymbol{H}^H(\boldsymbol{y})\boldsymbol{H}(\boldsymbol{y})\right)^{-1} \tilde{\boldsymbol{P}}^{1/2}, \tag{31}$$

where $\tilde{\boldsymbol{P}} = \mathrm{diag}\{\tilde{p}_1, \tilde{p}_2, \cdots, \tilde{p}_K\} \in \mathbb{C}^{K\times K}$ is a diagonal matrix with the $k$-th entry $\tilde{p}_k$ on its diagonal representing the power received at user $k$. To satisfy the constraint in (19b), we set $\tilde{p}_k = \gamma_k \sigma_k^2,\ \forall k \in \mathcal{K}$.

Since ZF beamforming projects each user's channel vector $\boldsymbol{h}_k(\boldsymbol{y})$ onto a subspace that is orthogonal to the other users' channel vectors, the inter-user interference is completely eliminated, i.e., we have $\boldsymbol{h}_k^H(\boldsymbol{y})\boldsymbol{w}_{k'} = 0$ for $\forall k' \neq k$. As a result, the objective function $\epsilon_k$ in (25) is simplified as

$$\epsilon_{k,\,\mathrm{ZF}} = \frac{1}{\gamma_k \sigma_k^2} \left|\boldsymbol{h}_k^H(\boldsymbol{y})\hat{\boldsymbol{w}}_k\right|^2 - 1, \quad \forall k \in \mathcal{K}. \tag{32}$$

Substituting (32) into (26a) and solving problem $(P_{\mathcal{H}})$, we obtain the surface shape of the FIM at a reduced complexity.

### C. Complexity Analysis

In this subsection, we evaluate the computational complexity of the proposed alternating optimization algorithm. In each iteration, the transmit beamforming optimization requires solving (20), (21), and (22), which have complexities of $\mathcal{O}\left(\left(N^3+6N^2\right)K\right)$, $\mathcal{O}\left((K+1)K^2\right)$, and $\mathcal{O}\left((4N+2)K^2\right)$, respectively. Moreover, updating the surface shape of the FIM involves calculating the gradients of $\nabla_{\boldsymbol{y}}\epsilon$, which has a complexity of $\mathcal{O}\left(4NLK^2\right)$. Note that some repeated matrix multiplications are only calculated once. As a result, the overall complexity order of Algorithm 1 is given by

$$\mathcal{O}\left(I_{\mathrm{AO}}\left[\left(N^3+6N^2\right)K + (3+K+4N+4NLI_{\mathrm{GA}})K^2\right]\right), \tag{33}$$

where $I_{\mathrm{AO}}$ and $I_{\mathrm{GA}}$ represent the number of iterations required for alternating optimization and gradient ascent, respectively.

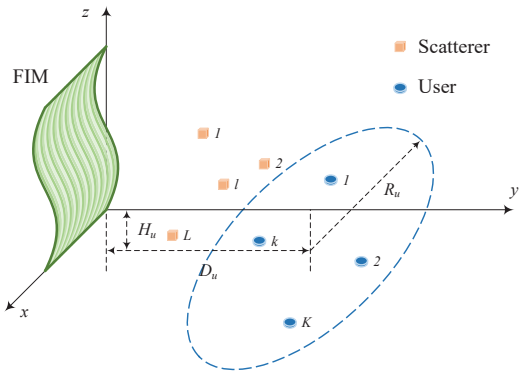


Fig. 3. An FIM-assisted multiuser downlink MISO communication system.

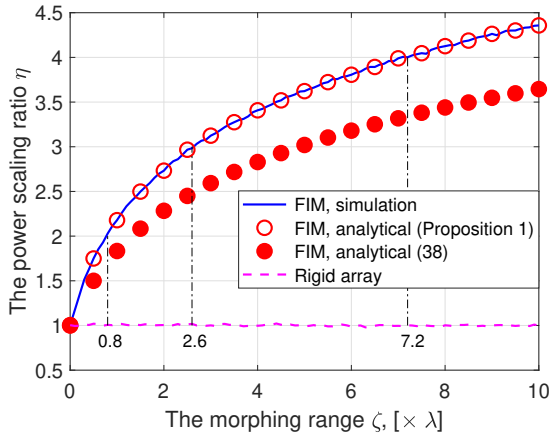


Fig. 4. The power scaling ratio $\eta$ versus the morphing range $\zeta$ of the FIM.

By contrast, using ZF transmit beamforming, as described in Section V-B, reduces the complexity to

$$\mathcal{O}\left(I_{\mathrm{AO}}\left[\left(N^3+4N^2+4NLI_{\mathrm{GA}}\right)K\right]\right). \tag{34}$$

Note that the complexities of both proposed methods are polynomial in $N$, $K$, and $L$.

## VI. Numerical Results

In this section, simulation results are presented to verify the benefits of deploying an FIM in wireless networks.

### A. Simulation Setup

Specifically, we consider a typical FIM-assisted single-cell network, as shown in Fig. 3. An FIM having $N = N_x N_z$ elements is deployed at the BS with the spacing between adjacent antennas being set to $d_x = d_z = \lambda/2$. The height of the BS is $H_u = 5$ meters (m), and $K$ users are uniformly distributed within a circular region on the ground with the radius of $R_u = 10$ m. The horizontal distance from the center of the circle to the BS is $D_u = 20$ m. Moreover, $L$ scatterers are uniformly distributed in the far field of the FIM, satisfying $\phi_\ell \sim \mathcal{U}[0,\pi)$ and $\theta_\ell \sim \mathcal{U}[0,\pi),\ \forall \ell \in \mathcal{L}$. Additionally, we assume that all the scatterers experience the same channel gain with $\rho_{k,\ell}^2 = \beta_k^2/L,\ \forall \ell \in \mathcal{L}$. The distance-dependent path loss is modeled as $\beta^2 = \beta_0^2 (d/d_0)^{-\bar{n}}$ [47], where $\beta_0^2 = (2\kappa d_0)^2$

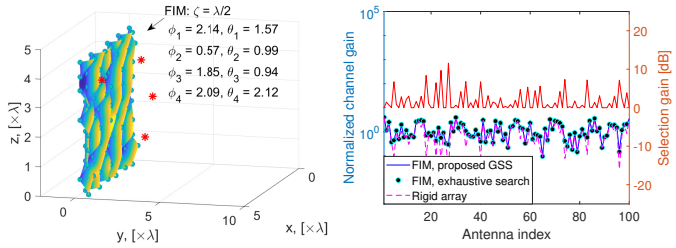


(a) (b)

Fig. 5. An FIM serving a single user, where $L = 4$, $\zeta = \lambda/2$. (a) The surface shape of the FIM; (b) Channel gain and selection gain across the FIM.

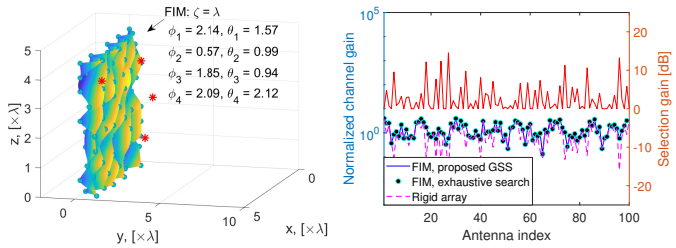


(a) (b)

Fig. 6. An FIM serving a single user, where $L = 4$, $\zeta = \lambda$. (a) The surface shape of the FIM; (b) Channel gain and selection gain across the FIM.

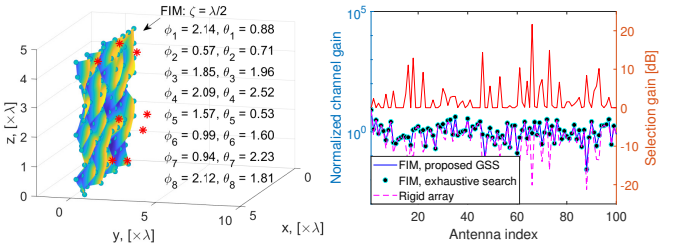


(a) (b)

Fig. 7. An FIM serving a single user, where $L = 8$, $\zeta = \lambda/2$. (a) The surface shape of the FIM; (b) Channel gain and selection gain across the FIM.

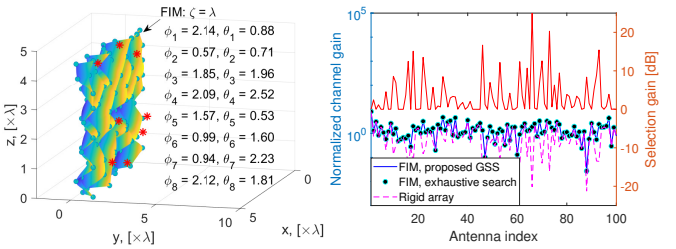


(a) (b)

Fig. 8. An FIM serving a single user, where $L = 8$, $\zeta = \lambda$. (a) The surface shape of the FIM; (b) Channel gain and selection gain across the FIM.

is the free space path loss at the reference distance of $d_0 = 1$ m, and $\bar{n}$ is the path loss exponent, which is set to $\bar{n} = 2.2$ for all users. We assume equal noise power for all the users, i.e., $\sigma_1^2 = \sigma_2^2 = \cdots = \sigma_K^2$. The noise spectral density is $-174$ dBm/Hz [37]. The system operates at 28 GHz with a bandwidth of 100 MHz.

Moreover, four transmission schemes are considered to evaluate the performance of the FIM:

- **ZF/MMSE with rigid array:** The ZF/MMSE transmit beamforming is utilized relying on a rigid 2D antenna array.
- **ZF/MMSE with FIM:** The surface shape of the FIM and transmit beamforming are alternately optimized. In each iteration, the ZF/MMSE beamforming is designed based on (31)/(20), while the FIM's surface shape is updated according to (29).

For the proposed alternating optimization algorithm, the maximum tolerable number of iterations is set to 100, and the convergence is determined if the fractional decrease of the transmit power is less than $-30$ dB. The parameter for relaxing the constraint (26c) is set to $\epsilon_{\min} = -5$. All simulation results are obtained by averaging over 100 independent channel realizations.

### B. Verification of the Analytical Results

We first consider a single-user scenario to demonstrate the accuracy of the analytical results derived in *Proposition 1*. To illustrate, we define the power scaling ratio $\eta = P_{\mathrm{r}}/\left(P_{\mathrm{t}} N \beta^2\right)$, since the impact of the large-scale path loss and the number of antennas has been well studied in conventional communication systems [48]. Fig. 4 shows the power scaling ratio $\eta$ versus the morphing range $\zeta$. We assume an infinite number of scatterers, resulting in Rayleigh fading for each channel. The spatial correlation between any two potential positions of each element is characterized by $r_{m,m'} = \mathrm{sinc}\left(\kappa d_{m,m'}/\pi\right)$ [19]. Compared to the conventional rigid array, the FIM is capable of significantly improving the channel gain. Specifically, the power scaling ratio $\eta$ logarithmically increases with the morphing range $\zeta$. For instance, an FIM having a morphing range of $\zeta = 0.8\lambda$ can boost the received signal power by 3 dB, while achieving 6 dB power gain may require a morphing range of $\zeta = 7.2\lambda$, which poses a great engineering challenge for the elasticity of the substrate. Additionally, the analysis provides a tight lower bound for all setups considered, with $\Delta(\zeta) < 0.75$ as observed in Fig. 4.

### C. The Morphing Capability of the FIM

Next, we characterize the performance improvement versus the FIM morphing capability, when considering a single user in the cell. Specifically, a square FIM having $N = 100$ elements is employed at the BS. We first consider a scenario having $L = 4$ scatterers that are randomly distributed in the front half-space of the FIM. The specific elevation and azimuth AoA from each scatterer are listed in the figure. We also assume that the normalized path gain is identical for the $L$ paths, i.e., $\alpha_{k,\ell} = 1/4$, $\ell = 1, 2, \cdots, 4$. Fig. 5(a) shows the optimal surface shape of the FIM when considering a morphing range of $\zeta = \lambda/2$. The red crosses represent the 'normalized locations' of the scatterers[6]. The optimal surface

[6]Note that in order to visualize the direction of the scatterers, we put all the scatterers on a sphere whose center point coincides with that of the FIM and its diameter is equal to the aperture of the FIM.

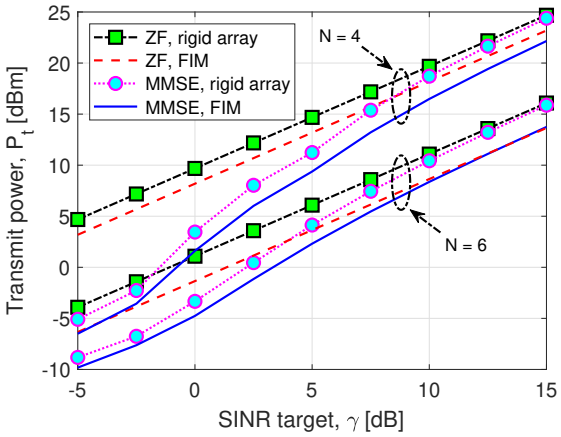


Fig. 9. Transmit power $P_{\mathrm{t}}$ versus the SINR target $\gamma$.

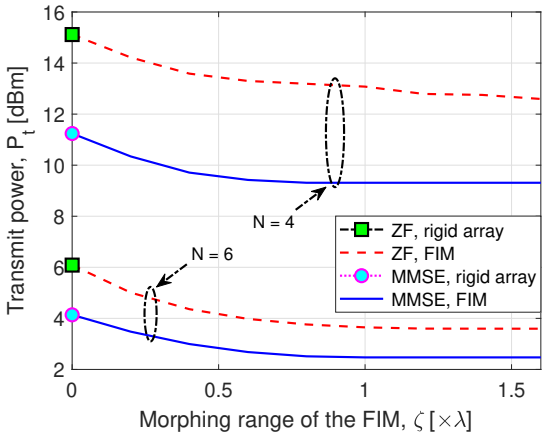


Fig. 11. Transit power $P_{\mathrm{t}}$ versus the morphing range of the FIM $\zeta$.

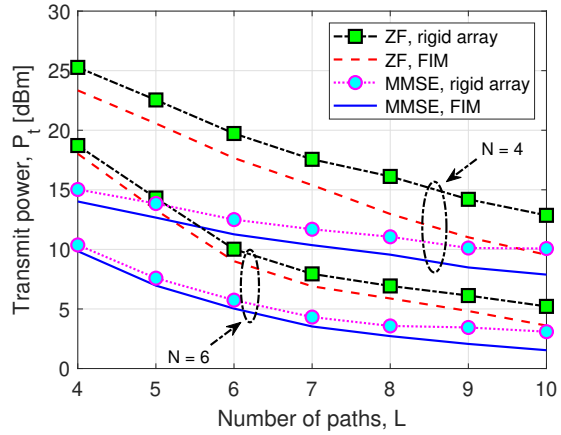


Fig. 10. Transmit power $P_{\mathrm{t}}$ versus the number of propagation paths $L$.

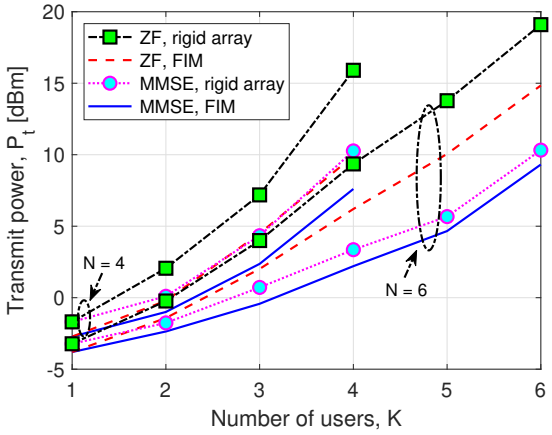


Fig. 12. Transmit power $P_{\mathrm{t}}$ versus the number of users $K$.

shape is obtained by dividing the morphing range $\zeta$ into $M = 4$ segments and applying the proposed GSS approach within each segment. Fig. 5(b) explicitly shows the channel gain associated with each antenna and the corresponding *selection gain*, which is defined as the ratio of the power received at the optimal position to that at the fixed antenna position. To verify the efficiency of the proposed method, we also compare it to the exhaustive search method that discretizes the morphing range into $10,000$ grid points and selects the position maximizing the channel gain for each element. The channel gain for a conventional system relying on a rigid 2D array is also plotted for comparison. As seen from Fig. 5(b), the FIM is capable of adapting its surface shape by positioning all the antenna elements at locations corresponding to the highest channel gain for the single-user case. Specifically, the FIM significantly improves the channel gain for the majority of elements and achieves the maximum selection gain of $11.58$ dB. Moreover, the proposed low-complexity GSS approach attains the same surface shape as the exhaustive search method.

In Fig. 6, we increase the morphing range of the FIM to $\zeta = \lambda$, while keeping the other parameters the same as in Fig. 5. This implies that the FIM has a larger space to morph its surface shape. We observe in Fig. 6(a) that some elements are positioned between $\lambda/2$ and $\lambda$ to enable the coherent superposition of signals from four directions. As a result, the maximum selection gain is increased to $14.52$ dB, as shown in Fig. 6(b). Furthermore, Figs. 7 and 8 examine the performance of the FIM in the presence of $L = 8$ scatterers in the propagation environment. The specific parameters of the eight scatterers are shown in the figures. Similarly, we assume $\alpha_{k,\ell} = 1/8,\ \ell = 1, 2, \cdots, 8$ for maintaining the normalized channel gain. The morphing range of $\zeta = \lambda/2$ is characterized in Fig. 7(a). Compared to Fig. 5(a), the FIM surface fluctuations are more erratic. This is because the presence of more scatterers results in the channels interfering constructively and destructively more frequently within the morphing range of the FIM. Due to the constructive superposition of more multipath propagation links, the overall channel gain across the FIM improves and the maximum selection gain increases to $21.65$ dB. Further increasing the morphing range to $\zeta = \lambda$ improves the highest selection gain to $24.94$ dB, as shown in Fig. 8. In all setups considered, the proposed low-complexity GSS approach achieves a performance comparable to the exhaustive search. In summary, the FIM performance gain increases with the morphing range $\zeta$ and the number $L$ of multipath propagation links.

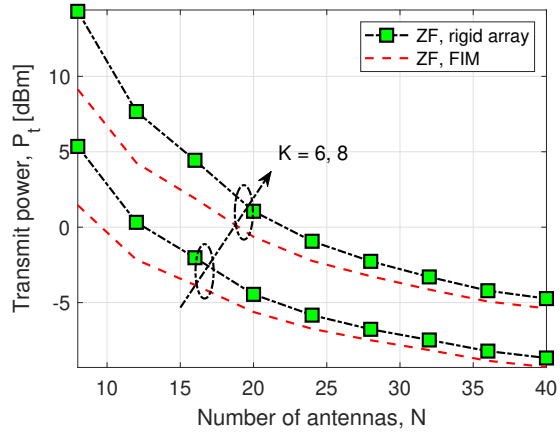


Fig. 13. Transmit power $P_{\mathrm{t}}$ versus the number $N$ of antennas, where ZF transmit beamforming is utilized.

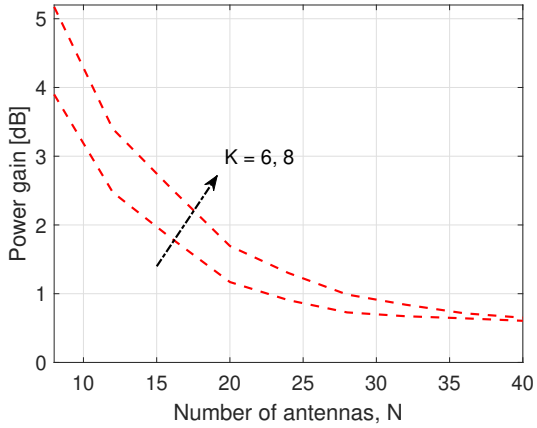


Fig. 15. Power gain versus the number $N$ of antennas, where ZF transmit beamforming is utilized.

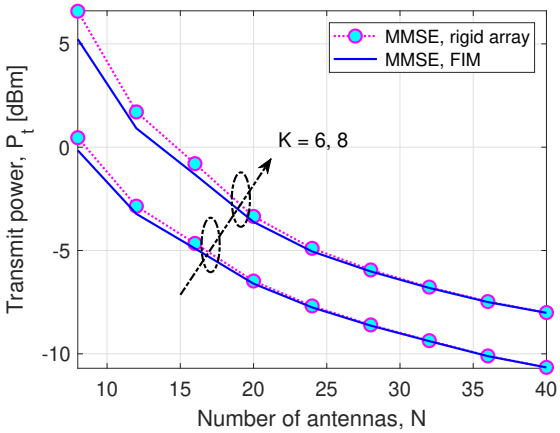


Fig. 14. Transmit power $P_{\mathrm{t}}$ versus the number $N$ of antennas, where MMSE transmit beamforming is utilized.

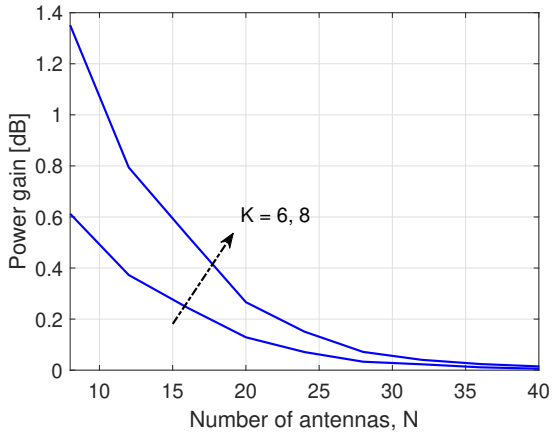


Fig. 16. Power gain versus the number $N$ of antennas, where MMSE transmit beamforming is utilized.

### *D. Performance versus Key System Parameters*

Next, we evaluate the performance of an FIM-based multiuser MISO system. For simplicity, we assume that all the users have identical rate requirements, i.e., $\gamma_k = \gamma,\ \forall k \in \mathcal{K}$. The alternating optimization algorithm proposed in Section V is utilized for optimizing the transmit beamformer and the FIM's surface shape for minimizing the transmit power at the BS. Fig. 9 shows the transmit power versus $\gamma$ for two different FIM sizes: *i)* $N = 4$, and *ii)* $N = 6$, assuming $N_x = 2$ in both cases. We also assume that there are $K = 4$ users and $L = 8$ propagation paths in the network. The morphing range of the FIM is set to $\zeta = \lambda$. Unsurprisingly, the MMSE beamformer performs best across the entire SNR range, while the ZF beamformer is asymptotically optimal at high SNR, where the noise is dominated by the interference [42]. As $N$ increases, the transmit power is further reduced, since the $K$ channels become asymptotically orthogonal. In all scenarios, the FIM provides an additional SNR gain by morphing its surface shape, further reducing the transmit power by about 3 dB.

Furthermore, Fig. 10 examines the performance as the number of propagation paths in the environment increases. We fix $\gamma = 5$ dB and keep all other parameters the same as in Fig. 9. Additionally, we consider $L \geq 4$ to guarantee that $\mathrm{rank}\left(\boldsymbol{H}\left(\boldsymbol{y}\right)\right) \geq K$ [8], [37]. It is shown that as $L$ increases, the performance improves, since the signal components of multiple propagation paths are more likely to form a favorable profile across the array. Moreover, the 3D FIM outperforms conventional rigid 2D arrays thanks to its morphing capability. Hence, the FIM may be beneficially morphed for counteracting the fading of wireless channels, and its performance gain becomes more significant as the number of propagation paths increases, indicating that multipath propagation is beneficial for FIM-assisted networks. By contrast, in the extreme case of strong LoS propagation, the FIM may hardly provide any performance gain.

In Fig. 11, we plot the transmit power of different schemes as the morphing range $\zeta$ increases, while setting $L = 8$ and keeping all other parameters the same. We note that the conventional 2D array is a special case of the FIM when $\zeta = 0$. As $\zeta$ increases, the FIM has more flexibility to adapt its surface shape, gradually reducing the transmit power required.

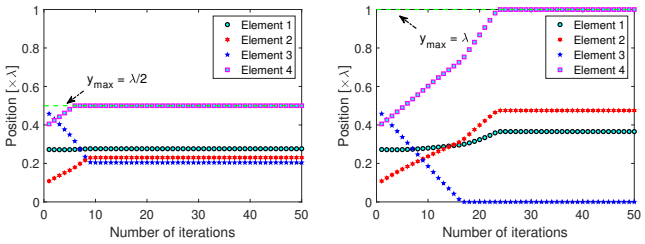


Fig. 17. Convergence of the FIM's surface shape, where (a) $L = 4$, $\zeta = \lambda/2$; (b) $L = 4$, $\zeta = \lambda$.

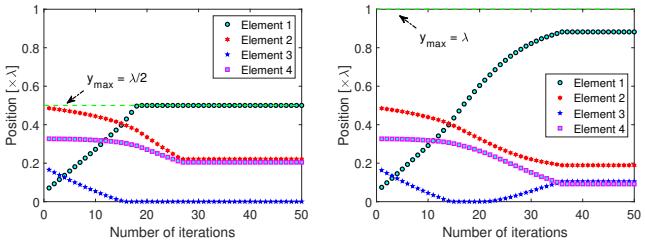


Fig. 18. Convergence of the FIM's surface shape, where (a) $L = 8$, $\zeta = \lambda/2$; (b) $L = 8$, $\zeta = \lambda$.

Nevertheless, we note diminishing returns, which is consistent with the logarithmic power scaling law derived in *Proposition 1*. For all setups, an FIM with a morphing range of $\zeta = \lambda$ may reduce the transmit power by about 3 dB. Moreover, it is interesting to observe that both increasing the number of antennas and the morphing range can narrow the gap between MMSE and ZF beamforming. This is due to the fact that the FIM improves the channel quality for each user and implicitly drives the system to operate in a higher SNR region.

Fig. 12 evaluates the transmit power versus the number of users $K$, when the morphing range of the FIM is set to $\zeta = \lambda$. It is observed that – as expected – more transmit power is required to meet the SINR requirements for a larger number of users. Moreover, interference mitigation is crucial in multiuser scenarios. In contrast to the ZF beamformer, which completely suppresses the multiuser interference, the MMSE beamformer strikes a favorable tradeoff between interference suppression and desired signal enhancement, while further reducing the transmit power. Under all the setups considered, the FIM is capable of adapting its surface shape for improving the channel orthogonality among the users as well as each user's channel quality. As a result, the FIM shows superior performance over the conventional benchmark schemes, with the performance gain increasing as the number of users increases. For instance, compared to the conventional ZF beamforming relying on a rigid 2D array, an FIM having $N = 4$ elements achieves a 6 dB power reduction, when serving $K = 4$ users. By contrast, when employing optimal MMSE beamforming, a 3 dB gain is observed over a rigid 2D array.

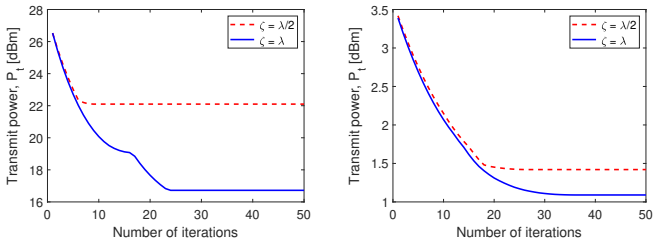


Fig. 19. Convergence of the transmit power, where (a) $L = 4$; and (b) $L = 8$.

### *E. Asymptotic Performance Analysis*

Next, we examine the asymptotic performance of the FIM as the number $N$ of antenna elements increases. Specifically, we set $N_x = 4$ and increase $N_y$ from 2 to 10. Two scenarios with *i)* $K = 6$ users and *ii)* $K = 8$ users are considered, both with SINR requirements of $\gamma = 5$ dB. We assume $L = 16$ propagation paths in the cell and set the morphing range of the FIM to $\zeta = \lambda$. The simulation results of utilizing ZF and MMSE beamforming schemes are shown in Figs. 13 and 14, respectively. We observe that as $N$ increases, the BS becomes capable of meeting the SINR requirements of multiple users with reduced power consumption, thanks to the array gain. However, serving a larger number of users requires consuming more transmit power at the BS. In all the setups considered, the FIM can further reduce the transmit power by flexibly morphing its surface shape according to the wireless propagation environment.

Furthermore, Figs. 15 and 16 show the corresponding power gain achieved by morphing the 3D surface shape of FIM. Note that the performance gain offered by the FIM decreases as $N$ increases. Nevertheless, we find that the power gain of the FIM is determined by the ratio of the number of antenna elements to the number of users, i.e., $N/K$. For a small number of users in the cell, increasing the number of antennas at the BS leads to *channel hardening*, which means that the channels associated with different users become mutually orthogonal. In this case, the performance improvement provided by the FIM is negligible compared to the gain from the large array aperture. However, when the number of users approaches the number of antennas, the gain of the FIM becomes more substantial. Observe from Figs. 15 and 16 that when $N/K = 1$, the power gains of the FIM are 5.17 dB and 1.35 dB for ZF and MMSE beamforming, respectively. The performance gain of the FIM is expected to be more significant when considering a larger number of scatterers or increasing the morphing range of the FIM. This warrants further research for accurately evaluating the asymptotic performance of the FIM with respect to various system parameters.

### *F. Convergence Analysis*

Finally, Figs. 17 $\sim$ 19 examine the convergence behavior of the proposed alternating optimization algorithm. The simulation setup is the same as for Fig. 11. We consider an FIM having $N = 4$ elements serving $K = 4$ users.

Specifically, Figs. 17 and 18 illustrate the evolution of the FIM's surface shape, as the iterations proceed, while the corresponding transmit power is shown in Fig. 19. Firstly, in Fig. 17(a), we consider a propagation environment having $L = 4$ scatterer clusters, and the morphing range is $\zeta = \lambda/2$. As expected, the FIM gradually reduces the transmit power, as observed in Fig. 19(a). However, due to the constrained morphing range, the position of element $4$ increases up to $y_{\max} = \lambda/2$, and the transmit power converges after $10$ iterations. When increasing the morphing range to $\zeta = \lambda$, element $4$ attains an improved morphing range to adapt its position. Interestingly, this also forces elements $1 \sim 3$ to re-adjust their positions for cooperatively reconfiguring the FIM's surface shape, further reducing the transmit power by about $5$ dB. The results considering $L = 8$ clusters of scatterers are shown in Fig. 18. In this case, the position of element $1$ is constrained by the morphing range of $\zeta = \lambda/2$ in Fig. 18(a). Further increasing the morphing range allows element $1$ to find an optimal position at $y_1 = 0.88\lambda$, as illustrated in Fig. 18(b). As a result, the transmit power is reduced from $1.4$ dBm to $1.1$ dBm. It is noted that in all the setups considered, the proposed alternating optimization method tends to converge within $30$ iterations. Furthermore, by comparing Fig. 19(a) and (b) we conclude that the transmit power reduces as the number of scatterers increases.

## VII. Conclusions

FIMs offer unprecedented flexibility in terms of both EM response and mechanical tuning. By morphing its surface shape, we have shown that an FIM deployed at a wireless BS is capable of significantly reducing the power consumption in wireless networks, while maintaining the same QoS requirements. Specifically, for a single-user scenario, each FIM element should adapt its position to maximize the channel gain. The optimal surface shape is determined by an efficient GSS approach. By contrast, for multiuser scenarios, the FIM's surface shape has to account for the SINR requirements of all the users. In this context, an efficient alternating optimization method has been customized for iteratively optimizing the FIM's surface shape and the transmit beamformer. Our analytical and simulation results have verified that the received power scales up logarithmically with the FIM's morphing range. Additionally, the numerical results have quantified the performance improvement of using an FIM over conventional rigid 2D arrays. An FIM with a morphing range of one wavelength, which corresponds to $10.8$ mm at $28$ GHz, results in a power gain of at least 3 dB.

Nevertheless, beneficially deploying FIMs in wireless networks also poses significant challenges. For instance, the surface shape morphing of a practical FIM may be hindered by hardware limitations and incur additional energy consumption, which motivates further research to develop efficient solutions for striking flexible performance, complexity, and overhead tradeoffs. Moreover, it warrants further investigations to examine the performance improvement brought about by FIM in terms of network capacity.

## Appendix A
## Proof of Proposition 1

Substituting $\boldsymbol{y}^{\mathrm{o}}$ into (17) yields

$$\begin{aligned} P_{\mathrm{r}} &= P_{\mathrm{t}} N \mathbb{E}\left(\left|h_{\tilde{n}}\left(y_{\tilde{n}}^{\mathrm{o}}\right)\right|^2\right) \\ &= P_{\mathrm{t}} N \mathbb{E}\left(\max_{0 \le y_{\tilde{n}} \le y_{\max}} \left|h_{\tilde{n}}\left(y_{\tilde{n}}\right)\right|^2\right), \end{aligned} \tag{35}$$

where $\tilde{n} \in \mathcal{N}$ represents an arbitrary element of the FIM.

Due to the challenge of explicitly calculating the expectation in (35), we instead derive a lower bound by examining a set of discrete sampling points in the interval $[0, y_{\max}]$. Specifically, we take $y_{\tilde{n},m} = m\lambda/2$ and thus $M = \lfloor \kappa\zeta/\pi \rfloor + 1$ represents the number of samples with $\lambda/2$ spacing.

Moreover, the instantaneous channel gain in (35) is lower bounded by

$$\max_{0 \le y_{\tilde{n}} \le y_{\max}} \left|h_{\tilde{n}}\left(y_{\tilde{n}}\right)\right|^2 \ge \max_{m=1,2,\cdots,M} \left|h_{\tilde{n}}\left(y_{\tilde{n},m}\right)\right|^2. \tag{36}$$

With half-wavelength sampling, $\left|h_{\tilde{n}}\left(y_{\tilde{n},m}\right)\right|^2$ are statistically independent of each other and each follows a Rayleigh distribution with the same mean value of $\beta^2$. According to Rényi's theory [49], we have

$$\max_{m=1,2,\cdots,M} \left|h_{\tilde{n}}\left(y_{\tilde{n},m}\right)\right|^2 \overset{d}{=} \beta^2 \sum_{m'=1}^{M} \frac{1}{1+M-m'} v_{m'}, \tag{37}$$

where $v_{m'}$ are i.i.d. standard exponential random variables with rate parameter $1$, $\overset{d}{=}$ indicates that two random variables have the same distribution properties.

As a result, we arrive at

$$\mathbb{E}\left(\beta^2 \sum_{m'=1}^{M} \frac{1}{1+M-m'} v_{m'}\right) = \beta^2 \sum_{m'=1}^{M} \frac{1}{1+M-m'} \tag{38}$$

$$\overset{M\to\infty}{\longrightarrow} \beta^2 \left(\log M + C\right). \tag{39}$$

Upon substituting (38) into (35) and using logarithmic interpolation, we obtain a lower bound on the received power. Upon numerically evaluating the performance gap caused by the scaling operation in (36), the proof is completed. ■

## References


[1] H. Tataria, M. Shafi, A. F. Molisch, M. Dohler, H. Sjöland, and F. Tufvesson, "6G wireless systems: Vision, requirements, challenges, insights, and opportunities," *Proc. IEEE*, vol. 109, no. 7, pp. 1166–1199, Jul. 2021.

[2] X. You, C.-X. Wang, J. Huang, X. Gao, Z. Zhang, M. Wang, Y. Huang, C. Zhang, Y. Jiang, J. Wang *et al.*, "Towards 6G wireless communication networks: Vision, enabling technologies, and new paradigm shifts," *Sci. China Inf. Sci.*, vol. 64, pp. 1–74, Nov. 2021.

[3] T. J. Cui, M. Q. Qi, X. Wan, J. Zhao, and Q. Cheng, "Coding metamaterials, digital metamaterials and programmable metamaterials," *Light Sci. Appl.*, vol. 3, no. 10, pp. e218–e218, Oct. 2014.

[4] J. An, C. Xu, Q. Wu, D. W. K. Ng, M. Di Renzo, C. Yuen, and L. Hanzo, "Codebook-based solutions for reconfigurable intelligent surfaces and their open challenges," *IEEE Wireless Commun.*, pp. 1–8, 2024, Early Access.

[5] M. Di Renzo, A. Zappone, M. Debbah, M.-S. Alouini, C. Yuen, J. de Rosny, and S. Tretyakov, "Smart radio environments empowered by reconfigurable intelligent surfaces: How it works, state of research, and the road ahead," *IEEE J. Sel. Areas Commun.*, vol. 38, no. 11, pp. 2450–2525, Nov. 2020.

[6] W. Tang, J. Y. Dai, M. Z. Chen, K.-K. Wong, X. Li, X. Zhao, S. Jin, Q. Cheng, and T. J. Cui, "MIMO transmission through reconfigurable intelligent surface: System design, analysis, and implementation," *IEEE J. Sel. Areas Commun.*, vol. 38, no. 11, pp. 2683–2699, Nov. 2020.

[7] J. An, C. Xu, L. Gan, and L. Hanzo, "Low-complexity channel estimation and passive beamforming for RIS-assisted MIMO systems relying on discrete phase shifts," *IEEE Trans. Commun.*, vol. 70, no. 2, pp. 1245–1260, Feb. 2022.

[8] Q. Wu and R. Zhang, "Beamforming optimization for wireless network aided by intelligent reflecting surface with discrete phase shifts," *IEEE Trans. Commun.*, vol. 68, no. 3, pp. 1838–1851, Mar. 2020.

[9] Z. Yu, J. An, E. Basar, L. Gan, and C. Yuen, "Environment-aware codebook design for RIS-assisted MU-MISO communications: Implementation and performance analysis," *IEEE Trans. Commun.*, pp. 1–15, 2024, Early Access.

[10] A. Zappone, M. Di Renzo, F. Shams, X. Qian, and M. Debbah, "Overhead-aware design of reconfigurable intelligent surfaces in smart radio environments," *IEEE Trans. Wireless Commun.*, vol. 20, no. 1, pp. 126–141, Jan. 2021.

[11] B. Sokal, P. R. B. Gomes, A. L. F. de Almeida, B. Makki, and G. Fodor, "Reducing the control overhead of intelligent reconfigurable surfaces via a tensor-based low-rank factorization approach," *IEEE Trans. Wireless Commun.*, vol. 22, no. 10, pp. 6578–6593, Oct. 2023.

[12] F. Saggese, V. Croisfelt, R. Kotaba, K. Stylianopoulos, G. C. Alexandropoulos, and P. Popovski, "On the impact of control signaling in RIS-empowered wireless communications," *IEEE Open J. Commun. Society*, vol. 5, pp. 4383–4399, May 2024.

[13] C. Pan, G. Zhou, K. Zhi, S. Hong, T. Wu, Y. Pan, H. Ren, M. Di Renzo, A. Lee Swindlehurst, R. Zhang, and A. Y. Zhang, "An overview of signal processing techniques for RIS/IRS-aided wireless systems," *IEEE J. Sel. Topics Signal Process.*, vol. 16, no. 5, pp. 883–917, Aug. 2022.

[14] S. Hu, F. Rusek, and O. Edfors, "Beyond massive MIMO: The potential of data transmission with large intelligent surfaces," *IEEE Trans. Signal Process.*, vol. 66, no. 10, pp. 2746–2758, May 2018.

[15] M. Cui, Z. Wu, Y. Lu, X. Wei, and L. Dai, "Near-field MIMO communications for 6G: Fundamentals, challenges, potentials, and future directions," *IEEE Commun. Mag.*, vol. 61, no. 1, pp. 40–46, Jan. 2023.

[16] J. An, C. Yuen, L. Dai, M. Di Renzo, M. Debbah, and L. Hanzo, "Near-field communications: Research advances, potential, and challenges," *IEEE Wireless Commun.*, vol. 31, no. 3, pp. 100–107, Jun. 2024.

[17] D. Dardari and N. Decarli, "Holographic communication using intelligent surfaces," *IEEE Commun. Mag.*, vol. 59, no. 6, pp. 35–41, Jun. 2021.

[18] A. Pizzo, L. Sanguinetti, and T. L. Marzetta, "Fourier plane-wave series expansion for holographic MIMO communications," *IEEE Trans. Wireless Commun.*, vol. 21, no. 9, pp. 6890–6905, Sep. 2022.

[19] J. An, C. Yuen, C. Huang, M. Debbah, H. V. Poor, and L. Hanzo, "A tutorial on holographic MIMO communications—part I: Channel modeling and channel estimation," *IEEE Commun. Lett.*, vol. 27, no. 7, pp. 1664–1668, Jul. 2023.

[20] ——, "A tutorial on holographic MIMO communications—part II: Performance analysis and holographic beamforming," *IEEE Commun. Lett.*, vol. 27, no. 7, pp. 1669–1673, Jul. 2023.

[21] ——, "A tutorial on holographic MIMO communications—part III: Open opportunities and challenges," *IEEE Commun. Lett.*, vol. 27, no. 7, pp. 1674–1678, Jul. 2023.

[22] D. Dardari, "Communicating with large intelligent surfaces: Fundamental limits and models," *IEEE J. Sel. Areas Commun.*, vol. 38, no. 11, pp. 2526–2537, Nov. 2020.

[23] M. Di Renzo and M. D. Migliore, "Electromagnetic signal and information theory," *IEEE BITS Inf. Theory Mag.*, pp. 1–13, Jan. 2024.

[24] J. An, C. Yuen, C. Xu, H. Li, D. W. K. Ng, M. Di Renzo, M. Debbah, and L. Hanzo, "Stacked intelligent metasurface-aided MIMO transceiver design," *IEEE Wireless Commun.*, vol. 31, no. 4, pp. 123–131, Aug. 2024.

[25] J. An, C. Xu, D. W. K. Ng, G. C. Alexandropoulos, C. Huang, C. Yuen, and L. Hanzo, "Stacked intelligent metasurfaces for efficient holographic MIMO communications in 6G," *IEEE J. Sel. Areas Commun.*, vol. 41, no. 8, pp. 2380–2396, Aug. 2023.

[26] C. Liu, Q. Ma, Z. J. Luo, Q. R. Hong, Q. Xiao, H. C. Zhang, L. Miao, W. M. Yu, Q. Cheng, L. Li *et al.*, "A programmable diffractive deep neural network based on a digital-coding metasurface array," *Nature Elect.*, vol. 5, no. 2, pp. 113–122, Feb. 2022.

[27] J. An, C. Yuen, Y. L. Guan, M. Di Renzo, M. Debbah, H. V. Poor, and L. Hanzo, "Stacked intelligent metasurface performs a 2D DFT in the wave domain for DOA estimation," in *Proc. IEEE Int. Conf. Commun.*, 2024, pp. 3445–3451.

[28] X. Ni, Z. J. Wong, M. Mrejen, Y. Wang, and X. Zhang, "An ultrathin invisibility skin cloak for visible light," *Sci.*, vol. 349, no. 6254, pp. 1310–1314, Sep. 2015.

[29] J. Cheng, S. Jafar-Zanjani, and H. Mosallaei, "All-dielectric ultrathin conformal metasurfaces: lensing and cloaking applications at 532 nm wavelength," *Sci. Rep.*, vol. 6, no. 1, p. 38440, Dec. 2016.

[30] S. M. Kamali, A. Arbabi, E. Arbabi, Y. Horie, and A. Faraon, "Decoupling optical function and geometrical form using conformal flexible dielectric metasurfaces," *Nature Commun.*, vol. 7, no. 1, p. 11618, May 2016.

[31] L. Cong, Y. K. Srivastava, A. Solanki, T. C. Sum, and R. Singh, "Perovskite as a platform for active flexible metaphotonic devices," *ACS Photo.*, vol. 4, no. 7, pp. 1595–1601, May 2017.

[32] C. Qian, B. Zheng, Y. Shen, L. Jing, E. Li, L. Shen, and H. Chen, "Deep-learning-enabled self-adaptive microwave cloak without human intervention," *Nature Photo.*, vol. 14, no. 6, pp. 383–390, Mar. 2020.

[33] C. Wang, Z. Lv, M. P. Mohan, Z. Cui, Z. Liu, Y. Jiang, J. Li, C. Wang, S. Pan, M. F. Karim *et al.*, "Pangolin-inspired stretchable, microwave-invisible metascale," *Adv. Materials*, vol. 33, no. 41, p. 2102131, Aug. 2021.

[34] C. Zhang, H. Dong, C. Zhang, Y. Fan, J. Yao, and Y. S. Zhao, "Photonic skins based on flexible organic microlaser arrays," *Sci. Adv.*, vol. 7, no. 31, p. eabh3530, Jul. 2021.

[35] X. Ni, H. Luan, J.-T. Kim, S. I. Rogge, Y. Bai, J. W. Kwak, S. Liu, D. S. Yang, S. Li, S. Li *et al.*, "Soft shape-programmable surfaces by fast electromagnetic actuation of liquid metal networks," *Nature Commun.*, vol. 13, no. 1, p. 5576, Sep. 2022.

[36] Y. Bai, H. Wang, Y. Xue, Y. Pan, J.-T. Kim, X. Ni, T.-L. Liu, Y. Yang, M. Han, Y. Huang *et al.*, "A dynamically reprogrammable surface with self-evolving shape morphing," *Nature*, vol. 609, no. 7928, pp. 701–708, Sep. 2022.

[37] D. Tse and P. Viswanath, *Fundamentals of Wireless Communication*. Cambridge University Press, 2005.

[38] K.-K. Wong and K.-F. Tong, "Fluid antenna multiple access," *IEEE Trans. Wireless Commun.*, vol. 21, no. 7, pp. 4801–4815, Jul. 2022.

[39] R. P. Brent, *Algorithms for Minimization without Derivatives*. Courier Corporation, 2013.

[40] R. W. Heath, N. González-Prelcic, S. Rangan, W. Roh, and A. M. Sayeed, "An overview of signal processing techniques for millimeter wave MIMO systems," *IEEE J. Sel. Topics Signal Process.*, vol. 10, no. 3, pp. 436–453, Apr. 2016.

[41] A. Shahmansoori, G. E. Garcia, G. Destino, G. Seco-Granados, and H. Wymeersch, "Position and orientation estimation through millimeter-wave MIMO in 5G systems," *IEEE Trans. Wireless Commun.*, vol. 17, no. 3, pp. 1822–1835, Mar. 2018.

[42] E. Björnson, M. Bengtsson, and B. Ottersten, "Optimal multiuser transmit beamforming: A difficult problem with a simple solution structure [lecture notes]," *IEEE Signal Process. Mag.*, vol. 31, no. 4, pp. 142–148, Jul. 2014.

[43] M. Bengtsson and B. Ottersten, "Optimum and suboptimum transmit beamforming," in *Handbook of Antennas in Wireless Communications*. CRC Press, 2001, pp. 18–1.

[44] A. Wiesel, Y. C. Eldar, and S. Shamai, "Linear precoding via conic optimization for fixed MIMO receivers," *IEEE Trans. Signal Process.*, vol. 54, no. 1, pp. 161–176, Jan. 2005.

[45] J. An, C. Xu, L. Wang, Y. Liu, L. Gan, and L. Hanzo, "Joint training of the superimposed direct and reflected links in reconfigurable intelligent surface assisted multiuser communications," *IEEE Trans. Green Commun. Netw.*, vol. 6, no. 2, pp. 739–754, Jun. 2022.

[46] J. An, M. Di Renzo, M. Debbah, H. V. Poor, and C. Yuen, "Stacked intelligent metasurfaces for multiuser downlink beamforming in the wave domain," 2023. [Online]. Available: https://arxiv.org/pdf/2309.02687.pdf

[47] T. S. Rappaport, G. R. MacCartney, M. K. Samimi, and S. Sun, "Wideband millimeter-wave propagation measurements and channel models for future wireless communication system design," *IEEE Trans. Commun.*, vol. 63, no. 9, pp. 3029–3056, Sep. 2015.

[48] H. Q. Ngo, E. G. Larsson, and T. L. Marzetta, "Energy and spectral efficiency of very large multiuser MIMO systems," *IEEE Trans. Commun.*, vol. 61, no. 4, pp. 1436–1449, Apr. 2013.

[49] A. Rényi, "On the theory of order statistics," *Acta Math. Acad. Sci. Hung*, vol. 4, no. 2, pp. 48–89, Sep. 1953.

**Jiancheng An** received the B.S. degree in Electronics and Information Engineering and the Ph.D. degree in Information and Communication Engineering from the University of Electronic Science and Technology of China (UESTC), Chengdu, China, in 2016 and 2021, respectively. From 2019 to 2020, he was a Visiting Scholar with the Next-Generation Wireless Group, University of Southampton, U.K. He is currently a research fellow with the School of Electrical and Electronics Engineering, Nanyang Technological University (NTU), Singapore. His research interests include stacked intelligent metasurfaces (SIM), flexible intelligent metasurfaces (FIM), and near-field communications.

**Chau Yuen** (S'02-M'06-SM'12-F'21) received the B.Eng. and Ph.D. degrees from Nanyang Technological University, Singapore, in 2000 and 2004, respectively. He was a Post-Doctoral Fellow with Lucent Technologies Bell Labs, Murray Hill, in 2005, and a Visiting Assistant Professor with The Hong Kong Polytechnic University in 2008. From 2006 to 2010, he was with the Institute for Infocomm Research, Singapore. From 2010 to 2023, he was with the Engineering Product Development Pillar, Singapore University of Technology and Design. Since 2023, he has been with the School of Electrical and Electronic Engineering, Nanyang Technological University. Dr. Yuen received IEEE Communications Society Fred W. Ellersick Prize (2023), IEEE Marconi Prize Paper Award in Wireless Communications (2021), and EURASIP Best Paper Award for JOURNAL ON WIRELESS COMMUNICATIONS AND NETWORKING (2021). He received the IEEE Asia Pacific Outstanding Young Researcher Award in 2012 and IEEE VTS Singapore Chapter Outstanding Service Award on 2019. He is a Distinguished Lecturer of IEEE Vehicular Technology Society, Top 2% Scientists by Stanford University, and also a Highly Cited Researcher by Clarivate Web of Science.

**Marco Di Renzo** (Fellow, IEEE) received the Laurea (cum laude) and Ph.D. degrees in electrical engineering from the University of L'Aquila, Italy, in 2003 and 2007, respectively, and the Habilitation à Diriger des Recherches (Doctor of Science) degree from University Paris-Sud (currently Paris-Saclay University), France, in 2013. Currently, he is a CNRS Research Director (Professor) and the Head of the Intelligent Physical Communications group in the Laboratory of Signals and Systems (L2S) at Paris-Saclay University – CNRS and CentraleSupelec, Paris, France. Also, he holds the 2023 France-Nokia Chair of Excellence in ICT at University of Oulu (Finland), he holds the Tan Chin Tuan Exchange Fellowship in Engineering at Nanyang Technological University (Singapore), and he was a Fulbright Fellow at The City University of New York (USA), a Nokia Foundation Visiting Professor at Aalto University (Finland), and a Royal Academy of Engineering Distinguished Visiting Fellow at Queen's University Belfast (U.K.). He is a Fellow of the IEEE, IET, EURASIP, and AAIA; an Academician of AIIA; an Ordinary Member of the European Academy of Sciences and Arts, an Ordinary Member of the Academia Europaea; an Ambassador of the European Association on Antennas and Propagation; and a Highly Cited Researcher. His recent research awards include the 2022 Michel Monpetit Prize conferred by the French Academy of Sciences, the 2023 IEEE VTS James Evans Avant Garde Award, the 2024 Best Tutorial Paper Award, and the 2024 IEEE COMSOC Marconi Prize Paper Award in Wireless Communications. He served as the Editor-in-Chief of IEEE Communications Letters during the period 2019-2023, and he is now serving on the Advisory Board. He is currently serving as a Voting Member of the Fellow Evaluation Standing Committee and as the Director of Journals of the IEEE Communications Society.

**Mérouane Debbah** (Fellow, IEEE) is a Professor at Khalifa University of Science and Technology in Abu Dhabi and founding Director of the KU 6G Research Center. He is a frequent keynote speaker at international events in the field of telecommunication and AI. His research has been lying at the interface of fundamental mathematics, algorithms, statistics, information and communication sciences with a special focus on random matrix theory and learning algorithms. In the Communication field, he has been at the heart of the development of small cells (4G), Massive MIMO (5G) and Large Intelligent Surfaces (6G) technologies. In the AI field, he is known for his work on Large Language Models, distributed AI systems for networks and semantic communications. He received multiple prestigious distinctions, prizes and best paper awards (more than 40 IEEE best paper awards) for his contributions to both fields He is an IEEE Fellow, a WWRF Fellow, a Eurasip Fellow, an AAIA Fellow, an Institut Louis Bachelier Fellow, an AIIA Fellow and a Membre émérite SEE. He is actually chair of the IEEE Large Generative AI Models in Telecom (GenAINet) Emerging Technology Initiative and a member of the Marconi Prize Selection Advisory Committee.

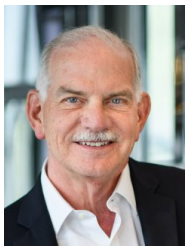

**H. Vincent Poor** (S'72, M'77, SM'82, F'87) received the Ph.D. degree in EECS from Princeton University in 1977. From 1977 until 1990, he was on the faculty of the University of Illinois at Urbana-Champaign. Since 1990 he has been on the faculty at Princeton, where he is currently the Michael Henry Strater University Professor. During 2006 to 2016, he served as the dean of Princeton's School of Engineering and Applied Science, and he has also held visiting appointments at several other universities, including most recently at Berkeley and Caltech. His research interests are in the areas of information theory, machine learning and network science, and their applications in wireless networks, energy systems and related fields. Among his publications in these areas is the book Machine Learning and Wireless Communications. (Cambridge University Press, 2022). Dr. Poor is a member of the National Academy of Engineering and the National Academy of Sciences and is a foreign member of the Royal Society and other national and international academies. He received the IEEE Alexander Graham Bell Medal in 2017.

**Lajos Hanzo** (FIEEE'04) received Honorary Doctorates from the Technical University of Budapest (2009) and Edinburgh University (2015). He is a Foreign Member of the Hungarian Science-Academy, Fellow of the Royal Academy of Engineering (FREng), of the IET, of EURASIP and holds the IEEE Eric Sumner Technical Field Award. For further details please see http://www-mobile.ecs.soton.ac.uk, https://en.wikipedia.org/wiki/Lajos_Hanzo.